Cement and Concrete Research 200 (2026) 108096

Contents lists available at ScienceDirect

Cement and Concrete Research

journal homepage: www.elsevier.com/locate/cemconres

Tailoring neutron-shielding boron-metakaolin geopolymers with B_4C filler: Surfactant-driven interfacial and microstructural control

Xiaobo Niu [a,*], Yogarajah Elakneswaran [a,*], Ryosuke Kikuchi [a], Ang Li [a], Sivasubramaniam Seralathan [a], Yoshihisa Hiraki [b], Junya Sato [b], Takeshi Osugi [b], Takashi Kamiyama [c], Brant Walkley [d]

[a] *Division of Sustainable Resources, Graduate School of Engineering, Hokkaido University, North 13, West 8, Sapporo, Hokkaido, 060-8628, Japan*
[b] *Waste Treatment Technology Section, Decommissioning Technology Department, Nuclear Backend Technology Center, Nuclear Fuel Cycle Engineering Laboratories, Japan Atomic Energy Agency, Japan*
[c] *Division of Quantum Energy Engineering, Graduate School of Engineering, Hokkaido University, North 13, West 8, Sapporo, Hokkaido, 060-8628, Japan*
[d] *School of Chemical, Materials and Biological Engineering, The University of Sheffield, Sir Robert Hadfield Building, Mappin Street, Sheffield, S1 3JD, UK*

ARTICLE INFO

Keywords:
Alkali-activated metakaolin-based geopolymer
Boron carbide
CTAB
Neutron shielding
Interface transition zone (ITZ)

ABSTRACT

The incorporation of boron (B) as a neutron absorber into metakaolin-based geopolymers for the remediation of radioactive debris following nuclear accidents has attracted considerable attention. In this study, boron carbide (B_4C) was employed as a functional filler, while cetyltrimethylammonium bromide (CTAB) acted as both a dispersant and a stabiliser to enhance the neutron shielding properties of metakaolin-based geopolymers. Although the addition of B_4C improved processability via a “roller-ball” effect and had no discernible impact on the geopolymerisation process, its weakly polar, negatively charged surface led to the formation of a loose, weak-shell interfacial transition zone (ITZ) between the filler and the matrix, thereby reducing mechanical strength and chemical stability. In contrast, CTAB self-assembled into an interdigitated monolayer on the B_4C surface, reversing its surface charge to positive and promoting its uniform dispersion within the matrix. While CTAB slightly inhibited the dissolution of metakaolin, it preferentially interacted with B_4C, thereby mitigating the adverse effects on the geopolymerisation process. Moreover, CTAB promoted gelation within the ITZ surrounding B_4C, facilitating the development of a dense, potassium-deficient, yet electrostatically stabilised microstructure. This synergistic interaction enhanced interfacial bonding between the filler and the matrix, enabled efficient stress transfer, and significantly improved mechanical performance and chemical stability. Furthermore, the B_4C–CTAB-modified geopolymers demonstrated enhanced neutron shielding performance. Overall, this work offers a promising approach for engineering high-performance, multifunctional geopolymer composites for nuclear and environmental applications.

1. Introduction

Following the Fukushima Daiichi (1F) accident, the core meltdown generated substantial quantities of radioactive waste, including fuel debris within the primary containment vessels (PCVs), contaminated water, and solid waste resulting from molten core–concrete interactions (MCCI) [1–3]. These wastes contain highly active fission products (e.g., Cs-137, Sr-90, Co-60, Se-79, and I-131) and continuously emit both gamma and neutron radiations [4,5]. Among these, neutron radiation presents a significant challenge in radioactive waste management and radiation protection due to its electrical neutrality, strong penetrating ability, and difficulty in shielding. Furthermore, neutron interactions with matter can induce secondary radiation by nuclear reactions, further increasing radiological hazards [6,7]. In biological systems, neutron radiation can trigger elemental transmutation, leading to the formation of secondary radioisotopes, severe internal irradiation, and potential DNA damage and genetic mutations [8–11]. Consequently, developing efficient and robust neutron-shielding binder materials is critically important for the safe disposal of complex radioactive waste streams.

Conventional neutron shielding binders used in nuclear waste encapsulation, such as heavy concrete and polyethylene, can attenuate neutron radiation to a certain extent [12,13]. However, their long-term

---

* Corresponding authors.
E-mail addresses: niuxiaobo@eng.hokudai.ac.jp (X. Niu), elakneswaran@eng.hokudai.ac.jp (Y. Elakneswaran).

https://doi.org/10.1016/j.cemconres.2025.108096
Received 28 May 2025; Received in revised form 20 October 2025; Accepted 20 November 2025
Available online 27 November 2025
0008-8846/© 2025 The Authors. Published by Elsevier Ltd. This is an open access article under the CC BY-NC-ND license (http://creativecommons.org/licenses/by-nc-nd/4.0/).

use in radiation environments is constrained by issues such as the risk of hydrogen explosions due to high water content, poor thermal stability, and degradation caused by ageing [14–16].In recent years, geopolymers—novel inorganic cementitious binders capable of replacing traditional Portland cement (OPC)—have attracted significant attention for nuclear waste encapsulation and radiation shielding. Among these, alkali-activated geopolymers have been the most extensively studied. These binders are produced through the depolymerisation of silica- and alumina-rich precursors (e.g., metakaolin, fly ash) in the presence of alkali activators, followed by polymerisation to form three-dimensional reticulated structures with high density, low permeability, and excellent chemical resistance and mechanical strength [15,16]. Studies have shown that cationic radionuclides such as Cs^+, Sr^{2+}, and Co^{2+} can be effectively immobilised in alkali-activated geopolymers through a multi-step ion exchange mechanism [17]. Additionally, in alkaline environments, Cs^+ forms stable complexes with zeolites derived from geopolymers, ensuring secure immobilisation [18]. In contrast, Sr^{2+} immobilisation in geopolymers occurs through the formation of (Na/K, Sr)-Al-Si gels and the physical encapsulation of excess $SrCO_3$ [19]. Furthermore, with appropriate tailoring, such as the incorporation of in situ-formed ettringite [20], alkali-activated geopolymers can be engineered to immobilise anionic radionuclides. Despite their excellent performance in immobilising radionuclides, geopolymers inherently lack efficient neutron shielding, which restricts their application in radioactive waste streams disposal. Therefore, enhancing the neutron absorption capacity of geopolymers through specific modifications is essential for expanding their use in this field.

In nuclear industry applications, boron (B) is widely used for neutron absorption and shielding due to the high neutron capture cross section of the isotope ^{10}B. This process involves the absorption of thermal neutrons, leading to the emission of lithium-7 and α particles [21]. In particular, boron is commonly employed in nuclear reactor cooling systems for reaction moderation and neutron flux control, typically in the form of boric acid (H_3BO_3) or boron carbide (B_4C) [22–24]. Inspired by these considerations, both boric acid and boron carbide have attracted attention for their potential in neutron absorption, particularly in the design of binder materials for the disposal of radioactive waste streams. In our previous study [25], we attempted to modify alkali-activated geopolymers using H_3BO_3 as the boron source. Although some BO_3 units in boric acid were converted to BO_4 units during the geopolymerisation process and were partially incorporated into the geopolymer matrix, concerns remain regarding key properties such as long-term stability and permeability resistance.

Alternatively, research on B_4C has primarily focused on its application as a filler in cementitious materials [26,27]. While these studies have demonstrated that incorporating B_4C filler can enhance the mechanical properties and neutron absorption capacity of cementitious materials, cementitious binders have inherent limitations compared to geopolymers for long-term radioactive waste streams disposal, primarily due to their chemical incompatibility with certain radionuclides and the presence of high free water content, which can induce problematic hydrogen generation [28]. Consequently, advancing research toward geopolymer-based neutron shielding systems is essential. However, studies on B_4C-containing geopolymer systems remain limited. Although a previous research has investigated B_4C-geopolymer composites fabricated under applied pressure [29], the stringent processing conditions and the absence of a fresh mortar stage hinder the development of geopolymer-based composites with B_4C as a filler. To address these challenges and enhance workability, current research focuses on activating aluminosilicate precursors with an alkali-activating solution (AAS) and incorporating B_4C filler to produce fresh mortars with high flowability. However, achieving a homogeneous and stable dispersion of B_4C in the system requires additional attention. This difficulty arises due to the low viscosity and surface tension of AAS containing dissolved aluminosilicate precursors in the early stages of geopolymerisation, as well as the poor suspension stability of the system [30]. To address this issue, selecting an appropriate dispersant is urgent. Cetyltrimethylammonium bromide (CTAB), a cationic surfactant, has been extensively studied in cement-based systems, including geopolymers, due to its ability to modify surface properties, enhance dispersion, and improve the overall performance of the material [31–33]. Structurally, CTAB comprises a hydrophilic quaternary ammonium head ($N^+(CH_3)_3$) with a bromide counterion (Br^-) and a hydrophobic long-chain alkyl tail ($C_{16}H_{33}$). This amphiphilic nature enables CTAB to interact effectively with both aqueous and solid phases, facilitating improved dispersion and stabilisation within the geopolymer matrix. Its applications on range geopolymers from controlling the rheology and workability of fresh pastes to influencing the microstructure and mechanical properties of the hardened matrix [34,35]. Furthermore, in the context of contamination mitigation, research has explored CTAB's adsorption potential, particularly for pollutants such as methylene blue [36] and tetracycline [37]. However, no studies have yet investigated the effectiveness of CTAB as a dispersant in B_4C-containing geopolymer systems to improve the homogeneity and stability of B_4C dispersion. Moreover, a comprehensive understanding of the effects of CTAB and B_4C incorporation on the geopolymerisation process and the properties of the hardened geopolymer composite remains lacking.

This study aims to develop highly mobile alkali-activated geopolymers with neutron absorption capability, incorporating B_4C as a boron-containing shielding filler. It investigates the role of CTAB in enhancing the dispersion and stability of geopolymer slurries containing B_4C filler, optimises the content ratio, and examines structural modifications in the geopolymer matrix, including the formation of interfacial transition zones (ITZs) between the matrix and filler. Geopolymerised systems with varying B_4C and CTAB contents are analysed to assess the effects of B_4C as a functional filler and CTAB as a stabiliser on geopolymerisation, using zeta potential, solubility, flowability and volume change measurements. The hardened samples are characterised via mechanical strength testing, X-ray diffraction (XRD), solid-state magic angle spinning nuclear magnetic resonance spectroscopy (MAS-NMR), field-emission electron probe microanalysis (FE-EPMA), transmission electron microscopy (TEM) and scanning transmission electron microscopy (STEM). The stability and structural integrity of CTAB-stabilised B_4C-containing geopolymers are evaluated through leaching experiments using inductively coupled plasma optical emission spectroscopy (ICP-AES). Finally, the neutron shielding properties of the hardened materials were evaluated using a compact neutron source driven by a set of electron linear accelerators. This study advances the development of neutron-shielding geopolymers by elucidating the effects of CTAB and B_4C on geopolymerisation processes, structural evolution within the geopolymer matrix, and the morphology of the matrix-filler interfacial transition zone. The findings offer valuable insights and practical implications for nuclear waste disposal, particularly in neutron-rich environments.

2. Experimental details

2.1. Materials

The metakaolin (SOBUECLAY-MK-13-SF-7) used for synthesising geopolymers was procured from Sobue Clay Co. Ltd. (Japan). Its median particle size (D50) was determined as 1.08 μm using X-ray transmission and 2.81 μm via laser diffraction. The chemical composition, analysed through X-ray fluorescence (XRF), is detailed in Table 1, with a silicon-to-aluminium molar ratio of approximately 0.98. The alkaline activator solution was prepared using potassium silicate solution (WAKO, Japan), which contained 29.1 wt% SiO_2, 21.9 wt% K_2O, and 49.0 wt% H_2O, along with potassium hydroxide (KOH, 86 wt%, WAKO, Japan) and ultrapure water. Boron carbide (B_4C, particle size: >95 % passing 45 μm, WAKO) was incorporated into the geopolymer formulation as a functional filler. Additionally, cetyltrimethylammonium bromide (CTAB, $C_{16}H_{33}N(CH_3)_3Br$, purity >96.0 %), supplied by Kanto Chemical CO.,

Table 1
Chemical composition (wt%) of the metakaolin as determined by X-ray fluorescence.

Component	Composition (wt%)
SiO_2	52.26
Al_2O_3	45.50
Fe_2O_3	0.45
TiO_2	1.12
CaO	0.08
MgO	0.05
K_2O	0.09
Na_2O	0.09
P_2O_5	0.12
L.O.I.*	0.23

* L.O.I. is loss on ignition at 1100 °C for 12 h.

INC., was employed as a dispersant and stabilising agent.

2.2. Samples preparation

The alkaline solution used for the synthesis of the geopolymer samples is defined as $1K_2O$: $1SiO_2$: $13H_2O$ (molar ratio). Geopolymer samples were prepared by mechanically mixing stoichiometric amounts of metakaolin with the alkaline solution to give $1Al_2O_3$: $K_2O = 1$. B_4C was added externally at 1, 5 and 10 wt% relative to the mass of metakaolin. For samples containing 10 wt% B_4C, CTAB was introduced at 3, 10 and 30 wt% relative to the added B_4C mass, denoted as the CTAB addition index of 3, 10, and 30, respectively. As a control, CTAB was also added to pure geopolymer samples (without B_4C) at an index of 30, corresponding to the CTAB amount used in samples with a hypothetical 10 wt% B_4C. The samples were labelled based on the amounts of B_4C and CTAB, as shown in Table 2. The Si/Al and B/Si ratios for each sample are also provided in the table. All weighed solids were first homogenised, then mixed with the alkaline activator solution and mechanically kneaded for 15 min to form a uniform slurry, followed by 15 min of vibration to remove entrained air before casting into moulds, following the same procedure as in our previous study [17,25], before being poured into the moulds. The fresh slurry was sealed in moulds and cured at 20 °C for 28 days. Subsequently, some samples designated for structural characterisation were dried in a thermostat at 40 °C for 24 h and then ground to a particle size of less than 150 μm. For morphological microscopy, samples were milled into two types of flakes: those with a thickness of less than 1 mm and those thinner than 100 μm.

Table 2
B_4C and CTAB contents of the samples, along with their corresponding CTAB index and major element ratios.

Samples	Liquid/ Solid (wt.)	CTAB index	B_4C (wt% of MK)	CTAB (wt% of B_4C)	Al/ Si	B/Si
Pure GP	1.733	N/A	0	0	0.678	0
B_4C-1 %	1.716	N/A	1	0	0.678	0.055
B_4C-5 %	1.651	N/A	5	0	0.678	0.275
B_4C-10 %	1.576	N/A	10	0	0.678	0.550
0.03CTAB-B_4C-10 %	1.571	3	10	3	0.678	0.550
0.1CTAB-B_4C-10 %	1.562	10	10	10	0.678	0.550
0.3CTAB-B_4C-10 %	1.534	30	10	30	0.678	0.550
0.3CTAB	1.683	30	0	30 (Assumed 10 % B_4C)	0.678	0

2.3. Assessment of B_4C and CTAB in geopolymerisation

The zeta potentials of individual B_4C particles, metakaolin particles, and their mixtures with varying concentrations of CTAB were measured using a zeta potential and particle size analyser (ELSZ-1000ZS, Otsuka Electronics, Japan). The measurements were conducted in solutions with pH values ranging from 6 to 12 and an ionic strength of 10 mM. The solid-to-liquid ratio of the suspensions was maintained at 1 g of B_4C or metakaolin per litre. CTAB concentrations were set at 0, 3, 5, 10, 20, and 30 wt%, based on the weight ratio of B_4C to the total mass in samples containing 10 % B_4C. Potassium nitrate (KNO_3, >99 %, KANTO, Japan) was used to regulate the ionic strength, while pH adjustments were made using KOH and HNO_3. Solubility experiments were conducted to assess the dissolution behaviour of metakaolin in alkaline solutions in the presence of B_4C and CTAB. The KOH solution had a concentration of 5 mol/L and a pH of 14.6 ± 0.05 at 25 °C. The solid-to-liquid ratio of metakaolin to solution in the dissolution test was 1:25, with B_4C added at 10 wt% of the metakaolin mass and CTAB at 30 wt% of the B_4C mass (index 30). Four dissolution systems were established: (i) metakaolin only, (ii) metakaolin with B_4C, (iii) metakaolin with CTAB, and (iv) metakaolin with both B_4C and CTAB. The dissolution process was carried out at 25 °C in a constant-temperature oven with continuous shaking. The test duration ranged from 10 min to 7 days. After the experiment, the solution was filtered through a 0.25 μm syringe filter. The concentrations of aluminium and silicon in the collected solutions were measured using inductively coupled plasma atomic emission spectrometry (ICP-AES, iCAP PRO, Thermo Fisher, USA). Slump flow experiments, conducted according to JASS 15 M-103 [38], using a Φ50 mm × H50 mm cylindrical mould, were performed with varying amounts of B_4C and CTAB. Slump flow values were measured at 0, 20, 60, and 120 min after mixing. The chemical deformation during the initial geopolymerisation phase (within the first seven days) was recorded for four sample types: pure geopolymer, samples containing the maximum content of B_4C (10 wt%), samples containing the maximum content of CTAB (30 wt%), and samples incorporating the maximum content of both B_4C and CTAB. The chemical deformation was determined by measuring variations in buoyancy, with reference to the general methodology described in ASTM C1608 [39]. Paraffin (Wako, Japan) was used as the immersion medium to facilitate the buoyancy measurements.

2.4. Characterisation of hardened samples

The compressive strength of the hardened geopolymer samples was measured in accordance with JIS A 1108 [40]. Cylindrical specimens with dimensions of Φ50 mm × 100 mm were used, as required by the test equipment regulations. For each experiment, three specimens were tested, and the average value was recorded. Thin 100 μm-level cross-sections were prepared from the middle region of each sample and embedded in resin on glass slides and examined under an optical microscope at 40× magnification. Further analysis was performed on optical micrographs of samples containing 10 wt% B_4C with varying CTAB index. The entire image area was divided into a 5 × 5 grid, and the spatial coordinates of B_4C particles were extracted using ImageJ. A heatmap illustrating the B_4C distribution was generated, and the variance of distribution frequency across the grid regions was subsequently calculated. All samples were characterised using a MultiFlex X-ray diffractometer (Rigaku, Japan) with CuKα radiation, operating in the 2θ range of 5–70°, at a scanning speed of 6.5° per minute and a step size of 0.02°. Solid-state magic angle spinning nuclear magnetic resonance (MAS NMR) spectra were collected using a Bruker 500 MHz spectrometer equipped with an 11.74 T magnet. For ^{27}Al MAS NMR, a 2.5 mm probe operating at 130.4 MHz was employed, with 90° pulse widths of 2.4 μs for metakaolin precursors and 3 μs for geopolymer samples, spinning at 30 kHz. Each sample underwent 3600 scans with a 1 s recycle delay. ^{29}Si MAS NMR spectra were acquired at 99.4 MHz using a

3.2 mm probe, with a 1.5 μs (30°) pulse width, a spinning speed of 5 kHz, and 2800 scans per sample, each with a 20 s recycle delay. ^{11}B MAS NMR spectra were recorded at 53.7 MHz with a 3.2 mm probe, a 2 μs (30°) pulse width, a 15 kHz spinning speed, and 720 scans per sample, each with a 5 s recycle delay. Chemical shifts for ^{27}Al, ^{29}Si, and ^{11}B nuclei were referenced to $AlCl_3$ solution (1 mol/L), $C_6H_{18}O_3Si_3$, and $NaBH_4$ respectively. The deconvolution of ^{29}Si MAS NMR spectra utilised a Gaussian amplitude function, while that of ^{27}Al and ^{11}B MAS NMR spectra incorporated quadrupolar interactions and employed multiple Pearson IV functions [41]. Polished 10 mm-level sections were examined using a field-emission electron-probe microanalyser (FE-EPMA, JXA-8530F, JEOL). An accelerating voltage of 15 kV and a beam current of 60 nA were used for X-ray mapping. The interface near the B_4C-geopolymer matrix in several target samples was microsampled using a focused ion beam scanning electron microscope (FIB-SEM, JEOL JIB-4600F). The sample preparation process is shown in Fig. S1. To mitigate damage from Ga^+ ion bombardment, a protective tungsten layer was deposited over the target phases. The samples were then cut into wedge-shaped sections approximately 15 μm wide, 2 μm thick, and 8 μm high. The sliced specimen was then lifted using an ex situ micromanipulator, attached to the tip of an OmniProbe® lift-out TEM grid (EM Japan Co., Ltd.), placed back into the FIB-SEM, and carefully trimmed to obtain a specimen thickness of less than ~150 nm. The final processed specimen was examined using a JEM-2010 (JEOL) transmission electron microscope (TEM) operated at 200 kV, equipped with a DV300W and a MultiScan Camera 794 (Gatan). The acquired TEM images and diffraction patterns were analysed using DigitalMicrograph® software (Gatan). Elemental distributions at the B_4C-geopolymer matrix interface were mapped using scanning transmission electron microscopy (STEM). The STEM analysis was performed using a Titan^3 G2 60–300 (Thermo Fisher Scientific, USA), operating at an accelerating voltage of 200 kV.

2.5. Evaluation in simulated environments

After 28 days of curing, semi-dynamic leaching tests were conducted at ambient temperature following the ANSI/ANS-16.1-2003 standard (American Nuclear Society, 2004) [42] to assess the stability of the samples in a simulated flowing groundwater environment. Fresh paste was cast into cylindrical moulds (1.5 cm in height, 1.3 cm in internal diameter), producing specimens with a surface area of 8.8 cm^2. Each specimen was immersed in 88 mL of ultrapure water as the leachant, maintaining a volume-to-surface-area ratio of 10 mL/cm^2. The leachates were collected and replaced at cumulative leaching time points of 2 and 9 h, and 1, 3, 5, 7, 14, 21, and 28 days. The collected leachates were analysed using inductively coupled plasma atomic emission spectroscopy (ICP-AES; SPECTROBLUE, Hitachi, Japan) over a wavelength range of 165–770 nm. To prevent sample degradation, all solutions used for ICP-AES measurements were acidified with 1 % HNO_3 (~60 wt%). Cumulative leached fractions were calculated by summing the total amount leached up to each specified time point.

Samples with and without B_4C (10 wt% of MK) and CTAB (30 wt% of B_4C) were prepared in varying thicknesses for neutron shielding experiments (Table S1). Neutron imaging was conducted at the AISTANS facility at the Tsukuba Centre, National Institute of Advanced Industrial Science and Technology (AIST), Japan. This compact accelerator-based facility features an electron linear accelerator that stably generates high-quality cold neutron pulse beams suitable for various neutron imagings (Fig. S2). The neutron transmission measurement was performed using a neutron flat panel detector (nFPD) with a 14 × 17-in. active area, 139 μm pixel size, and a LiF/ZnS scintillator. Images were acquired via direct optical coupling with an exposure time of 10 s per frame. The acquired neutron transmission images were subsequently processed using ImageJ software. Grayscale intensity values along specific horizontal scan lines were extracted to evaluate spatial variations in neutron attenuation across the samples.

3. Results and discussion

3.1. Effect of CTAB on charge alteration

Fig. 1 (a) illustrates the zeta potential of metakaolin (MK) and B_4C in the presence or absence of CTAB as a function of ambient solution pH. In the absence of CTAB, B_4C exhibited a negative charge within the equilibrium pH range of 6–12, which increased slightly as pH rose. This behaviour occurred because, although B_4C was largely insoluble in aqueous solutions, particularly in alkaline conditions, its surface underwent partial oxidation and hydroxylation [43], leading to the formation of B_2O_3 and subsequently negatively charged -$B(OH)_4^-$ or -BO_2^- species with high hydroxyl group concentrations. Similarly, without CTAB, MK also exhibited an increasingly negative charge as pH increased, consistent with previous findings [44], which attributed this trend to the deprotonation of surface Si-OH groups. In contrast, when CTAB was introduced at a concentration of 30 index units, the zeta potential of both MK and B_4C reversed to a positive value and demonstrated a pH-independence within this range. Fig. 1 (b) depicts the variation in zeta potential of MK and B_4C as a function of CTAB content at a constant pH (~12). The zeta potential of B_4C exhibited a two-phase change: initially, it started at approximately −15 mV and increased rapidly with rising CTAB content until index 10, after which it stabilised at around 45 mV. In contrast, the zeta potential of MK followed a three-stage progression. In the first stage, when the CTAB content was below index 10, the negative charge gradually decreased until reaching the isoelectric point. In the second stage (index 10–20), the zeta potential increased rapidly, crossing the isoelectric point and changing into positive. Finally, beyond index 20, the rate of increase slowed, eventually plateauing around index 30.

To further examine the influence of CTAB on particle surface charge, the electrostatic potentials of several possible CTAB species in aqueous solution were calculated via density functional theory (DFT), as shown in Fig. 1(c). All calculations were performed using the Gaussian 16 software package with the B3LYP functional and 6-31G(d,p) basis set. Implicit solvation was applied using the self-consistent reaction field (SCRF) model with water as the solvent. Molecular geometries were specified using the connectivity option. When CTAB is completely non-ionised (Fig. 1(c)-1), the long-chain alkyl mid-section remains neutral. However, at the quaternary ammonium end, Br^- adsorption occurs due to electrostatic interactions, resulting in a localised negative charge near Br^- and a positive charge at the distal quaternary ammonium site. In aqueous solution, Br^- ionises, allowing CTAB to exist as a free quaternary ammonium cation (Fig. 1(c)-2 and 3). Ideally, when ionised CTAB remains in a linear configuration, its quaternary ammonium end carries a strong positive charge, which gradually diminishes toward neutrality along the alkyl chain (Fig. 1(c)-2). However, due to the polarity of the aqueous environment, the alkyl chain tends to curl and fold because of hydrophobic interactions and van der Waals forces [45]. In this case, the calculated electrostatic potential of CTAB ions exhibits a strong positive charge at the quaternary ammonium end, gradually decreasing along the alkyl chain, though maintaining an overall positive charge (Fig. 1(c)-3). Therefore, the CTAB studied in these systems is fundamentally positively charged and adopts a strongly positively charged configuration at its quaternary ammonium cation end.

When CTAB coexisted with B_4C at an index below 10, free CTAB ions rapidly adsorbed onto the B_4C surface, forming an interdigitated monolayer (Fig. 1(b)). B_4C was inherently hydrophobic due to its uniform surface charge distribution, which arose from its high covalency and absence of hydrophilic functional groups [46]. Consequently, CTAB adsorption on the B_4C surface was driven by electrostatic interactions, which oriented the quaternary ammonium cation toward the surface, and hydrophobic interactions, which oriented the alkyl chain outward. This adsorption behaviour had been previously observed in studies of carbon nanomaterials (CNMs) [47]. As the CTAB concentration increased beyond an index of 10, additional CTAB did not further

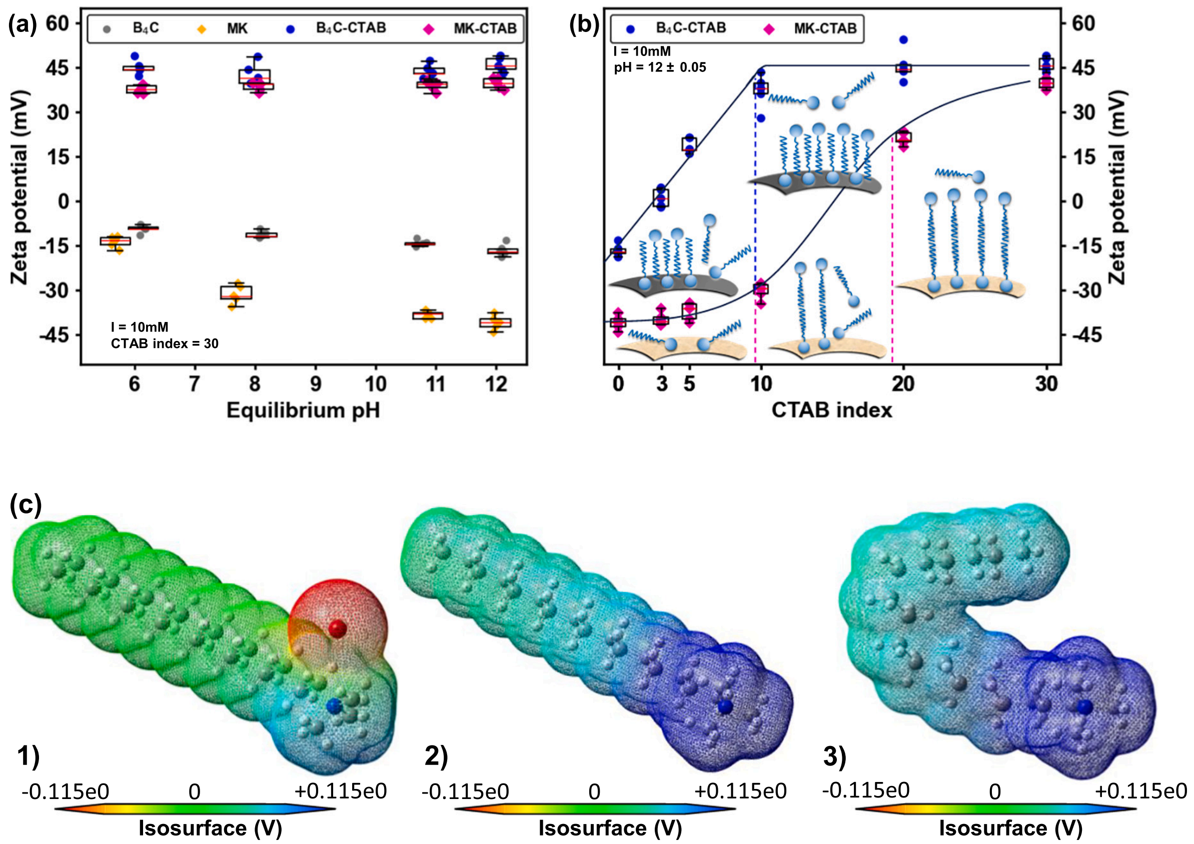

Fig. 1. Zeta potential of (a) MK and B_4C with (index = 30) or without CTAB, (b) MK and B_4C at varying levels of CTAB. The boxes depict the interquartile range (IQR), encompassing the data between the 25th percentile (Q1) and the 75th percentile (Q3).The red line within each box denotes the median (50th percentile). Whiskers extend to the furthest data points lying within 1.5 times the IQR below Q1 and above Q3, respectively. (c) the electrostatic surface potentials (V) of CTAB for 1) molecules, 2) ions in solution, and 3) ions in highly concentrated salt solutions were calculated using first-principles methods. (For interpretation of the references to colour in this figure legend, the reader is referred to the web version of this article.)

enhance the positive charge of B_4C. This suggested that the interdigitated monolayer adsorbed on the B_4C surface reached saturation at this concentration, making further structural modifications difficult and thereby limiting any additional effect on the zeta potential. Correspondingly, when the CTAB index was below 10, the adsorption of CTAB led to a much slower increase in the zeta potential of MK (Fig. 1(b)). This is attributed to the hydrophilicity imparted by the Si–OH groups on the MK surface, which facilitated a hydrophilic interaction between CTAB and the surface, with the quaternary ammonium cation head group oriented accordingly. Although the terminal end of the alkyl chain carried some positive charge (Fig. 1(c)), the primary source of positive charge was inwardly oriented, resulting in a slower overall increase in the zeta potential of MK. As the CTAB index increased further, interactions among the hydrophobic tail groups induced the formation of a bilayer on the MK surface. At this stage, the quaternary ammonium cation groups faced outward, leading to a rapid increase in the zeta potential of MK, shifting from negative to positive. Subsequently, as more CTAB was introduced, the bilayer structure reached its capacity, preventing further adsorption. Consequently, the increase in zeta potential plateaued with additional CTAB. This S-shaped curve observed with increasing CTAB concentration was consistent with previous studies [48].

3.2. Effect of CTAB on the initial geopolymerisation stage

3.2.1. Dissolution process of MK and B_4C during geopolymerisation

Fig. 2 presents the time series of Al and Si concentrations dissolved in KOH solution, along with B concentrations released from B_4C, under

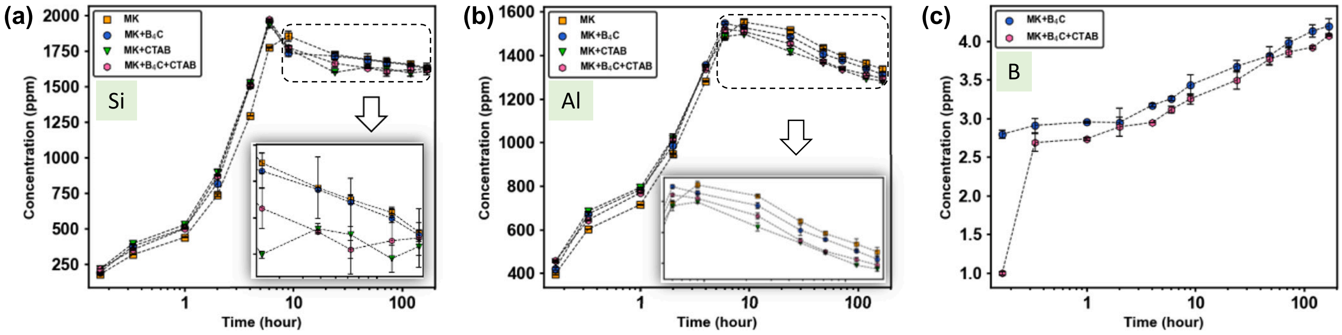

Fig. 2. Time series of (a) Al, (b) Si, and (c) B concentrations following dissolution in KOH solution.

different conditions: with or without B_4C and CTAB. The dissolution process of MK occurred in two distinct phases. During the first 8–10 h, the concentrations of Al and Si gradually increased, reaching their peak before declining. This trend arose because MK dissolved rapidly in the early stages of geopolymerisation, releasing Al and Si into the solution. However, as the reaction progressed, free Al and Si participated in polymerisation, forming precipitates and thereby reducing their concentrations in solutions [49]. Compared to the MK-only system, where the concentration peak appeared at 10 h, all other systems exhibited an earlier peak at 8 h. Notably, Si reached a higher peak concentration in these systems (Fig. 2(a)). This suggests that the presence of either B_4C or CTAB facilitated the early dissolution of MK, likely by enhancing the dispersion of MK particles. In the second phase, Al and Si concentrations stabilised due to the dynamic balance between dissolution and precipitation. At equilibrium, the MK-only system exhibited the highest concentrations of Al and Si (Fig. 2(a) and (c)). In contrast, the addition of CTAB reduced these concentrations, likely because CTAB adsorbed onto the MK surface, partially inhibiting its dissolution. The lowest Al and Si concentrations were observed in the system without B_4C, suggesting that in its absence, more CTAB accumulated on the MK surface, further hindering dissolution. Even though the variations between the systems appear minor, these trends remain scientifically relevant and are further examined through complementary analyses in the following sections. In addition, a small amount of B was dissolved from B_4C, and the presence of CTAB further reduced its concentration in the system (Fig. 2(c)). This confirms that CTAB adsorbs onto the surface of B_4C, partially inhibiting its dissolution.

3.2.2. *Flowability*

The workability and flowability of the fresh geopolymer pastes were assessed through slump flow experiments (Fig. 3). All samples exhibited consistent flowability for up to one hour after mixing, followed by a significant decline in the subsequent hour. This behaviour can be attributed to the induction phase during the first hour, when the dissolution of silicates and aluminates keeps them in a dispersed state. Over time, Si and Al monomers or oligomers undergo polycondensation reactions, leading to the formation of a silica-alumina polymer network. This transition gradually converts the system from a suspension to a gel, resulting in reduced flowability [50]. An increase in B_4C content enhanced the initial flowability of the paste while mitigating the subsequent decline in flowability during the second phase (Fig. 3(a)). This effect is attributed to the “roller-ball” mechanism [51], where B_4C, as an inert phase, reduces particle friction and interparticle bonding during shear, thereby lowering shear resistance and improving flowability.

Similarly, the introduction of CTAB into the geopolymer system further enhanced overall flowability and significantly slowed the rate of flowability loss (Fig. 3(b)). Specifically, in samples with 10 wt% B_4C, flowability improved as CTAB content increased. However, in samples with the same CTAB level, those without B_4C experienced an even greater improvement in flowability. This suggests that while CTAB substantially improves the flowability of fresh geopolymer paste and delays the setting time, the effect is somewhat moderated by the presence of B_4C. This phenomenon may arise because CTAB accumulates around MK particles via electrostatic interactions, enhancing their dispersibility but simultaneously reducing their dissolution rate and contact with other oligomers. In the presence of B_4C, a portion of CTAB preferentially associates with B_4C surfaces, thereby diminishing its influence on MK. These findings align with the zeta potential measurements (Fig. 1) and solubility experiments (Fig. 2). It is worth noting that, although the liquid-to-solid (L/S) ratio (Table 2) is generally considered a key parameter influencing flowability, no clear correlation was observed in this study. For example, the pure geopolymer with the highest L/S ratio exhibited the lowest flowability and the shortest setting time (Fig. 3(a)). This suggests that the variations in flowability are not primarily governed by the L/S ratio. Instead, the effects of B_4C and CTAB appear to play a more dominant role in controlling the rheological behaviour of the fresh geopolymer paste.

3.2.3. *Chemical deformation*

Fig. 4 illustrates the chemical deformation of the samples over a 7-day period. All samples in this study exhibited a stepwise volumetric expansion. Previous studies have reported that Na-based metakaolin geopolymers typically undergo a three-stage chemical deformation

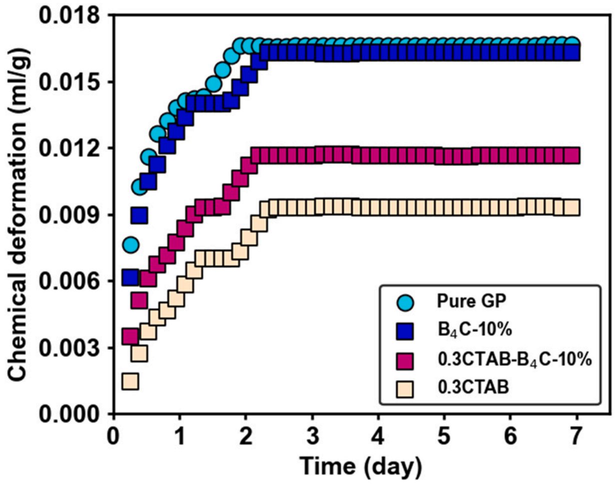

Fig. 4. Chemical deformation of geopolymer samples as a function of time.

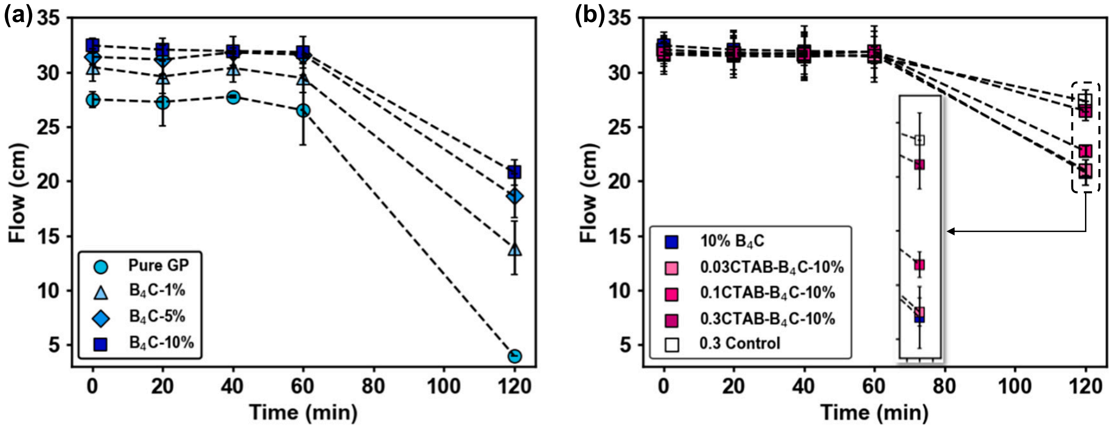

Fig. 3. Slump flow diameter over time for geopolymer samples (a) without CTAB and (b) with CTAB.

(shrinkage–expansion–shrinkage) [52]. In contrast, for the present K-based systems, no clear initial shrinkage stage was observed. It is believed that this early shrinkage, likely caused by the rapid dissolution of MK, may have been very short in duration and already completed during the 15 min mixing and 15 min vibration prior to the onset of measurements. This difference can be reasonably attributed to the larger ionic radius of K^+ compared to Na^+, which is also consistent with the much higher flowability of K-based fresh pastes. Moreover, unlike in Na-based systems, no final shrinkage stage associated with the recombination and polymerisation of Al-rich species with silicate oligomers into Si-rich amorphous gels was observed, again likely reflecting the distinct role of K^+ as a charge-balancing cation.

The initial swelling observed in the K-based geopolymerisation process is generally attributed to the adsorption of a large amount of water by the K-A-S-H gel phase formed during polymerisation, leading to system expansion [53]. Following this initial swelling phase, a brief plateau occurred, likely due to the consumption of free water by alkali–silica reaction gel [54], which may be present in the system at this stage. This depletion of free water halted gel swelling, resulting in a temporary stabilisation of volume. After this plateau, continued swelling was observed, potentially driven by factors such as new gel precipitation, additional hydration reactions, and pore water redistribution [55]. This process persisted until the gel network was largely established and the migration of alkali ions (K^+) reached equilibrium. The addition of B_4C had minimal impact on overall volume expansion, though it slightly delayed the onset of the second solubilisation compared to the pure geopolymer. This indicates that B_4C, as an inert phase, did not significantly modify the gel structure or pore characteristics of the matrix, although it may have slowed the initial geopolymerisation reaction. In contrast, the addition of CTAB significantly suppressed sample expansion, with this effect being more pronounced in the absence of B_4C. This suppression was likely due to the formation of CTAB micelles, which substantially increased matrix porosity. The additional pores created a "buffer zone" that absorbed internal strain, thereby reducing macroscopic expansion by accommodating volume changes induced by gel formation and water-absorption swelling. However, in the presence of B_4C, the overall deformation in the matrix was reduced, likely due to the aggregation of CTAB near the B_4C particles, which decreased porosity and consequently weakened its expansion inhibition.

3.3. Microstructural and mechanical properties

Fig. 5(a) illustrates the macroscopic dispersion of cylindrical specimens after 28 days of curing, along with the microdispersion of their cross-section, observed using an optical microscope at 40× magnification (sampled horizontally at the cylinder's centre). Due to its high specific gravity and low dispersion stability, B_4C exhibited significant sedimentation and uneven distribution under gravitational influence (Fig. 5(a)-1–3). With increasing CTAB content, the dispersion progressively improved, achieving uniformity at a CTAB index of 30 (Fig. 5(a)-5–7). These microscopic observations were quantified in Fig. 5(b), which presents heatmaps and distribution frequency variance derived

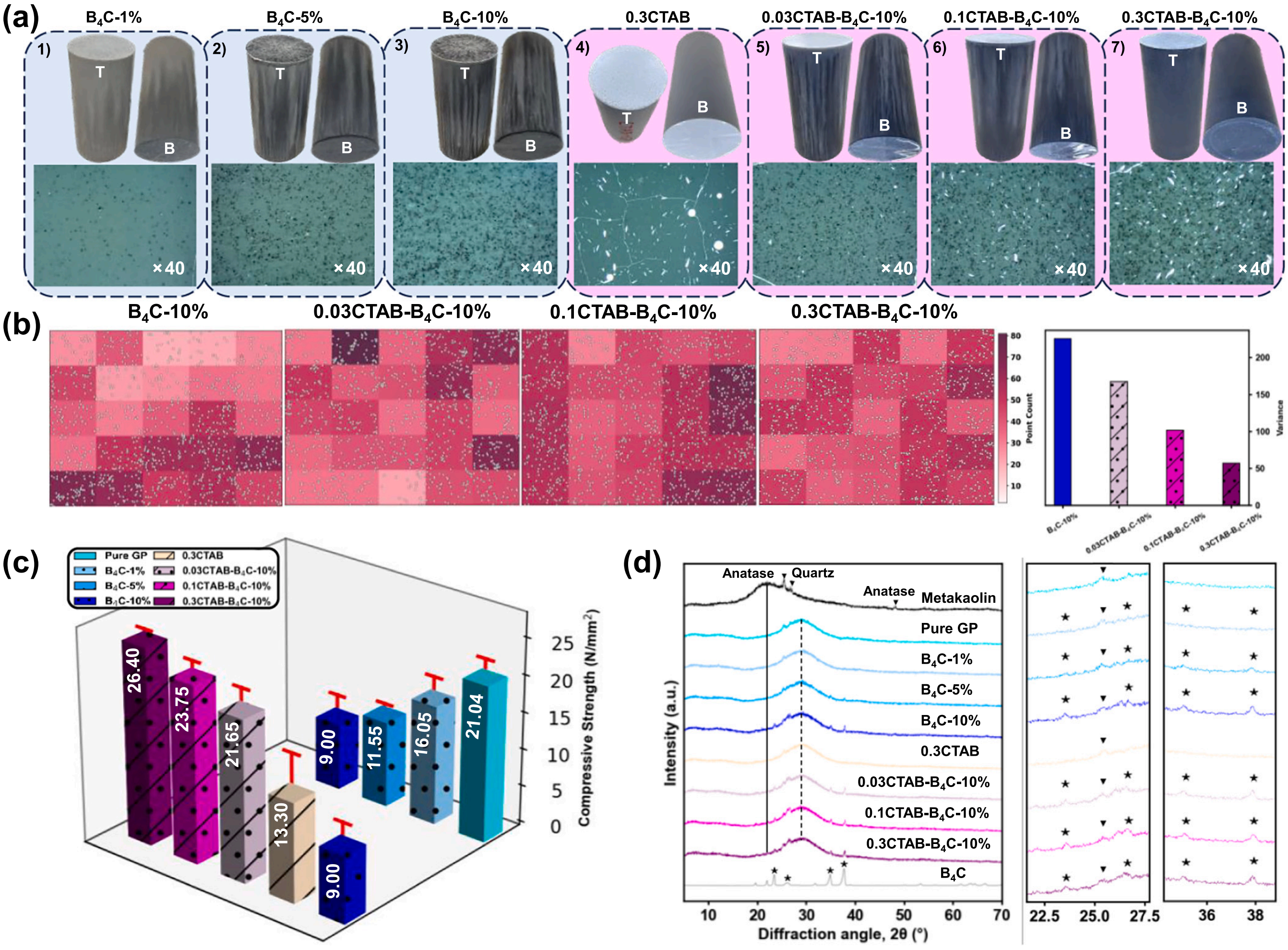

Fig. 5. (a) macro- and micro-dispersion, (b) heatmap of dispersion and variance in the samples containing 10 wt% B_4C, (c) uniaxial compressive strength, and (d) X-ray diffraction (XRD) patterns of hardened samples cured for 28 days.

from optical microscope images. The results confirm that CTAB effectively enhanced the uniformity of B_4C dispersion, with the most homogeneous distribution observed at the CTAB index of 30. Additionally, the B_4C packing density within the field of view increased with B_4C content. Meanwhile, sample porosity rose with higher CTAB levels, as micelle formation from the hydrophobic tails of CTAB hindered gelation in the central region. However, the presence of B_4C at the same CTAB level partially mitigated this porosity increase, a result consistent with the chemical deformation trends shown in Fig. 4.

Fig. 5(c) presents the uniaxial compressive strength of the samples. After 28 days of curing, the pure geopolymer cylindrical specimens exhibited a compressive strength of approximately 20 N/mm^2. With the incorporation of B_4C, the compressive strength progressively decreased, falling below 10 N/mm^2 for specimens containing 10 wt% B_4C. This reduction can be attributed to two primary factors. First, B_4C is chemically inert in highly alkaline environments, meaning that its interaction with the geopolymer matrix is predominantly physical rather than chemical. Additionally, the negatively charged and hydrophobic surface of B_4C particles leads to weak interfacial bonding with the matrix (Fig. 1). Second, B_4C particles have a tendency to agglomerate and precipitate during mixing and curing, leading to the formation of filler-rich, matrix-deficient regions. These localised inhomogeneities introduce structural defects and reduce the amount of geopolymer gel in certain areas, ultimately weakening the overall mechanical strength of the material. When CTAB was added to the geopolymers, the compressive strength decreased, primarily due to a significant increase in porosity caused by the introduction of numerous air bubbles (Fig. 5(a)-4). Interestingly, however, in samples containing 10 wt% B_4C, the addition of CTAB led to a notable increase in compressive strength—surpassing that of the pure geopolymer at the lowest CTAB concentration and reaching up to 24 N/mm^2—even though CTAB also increased porosity in these samples. This enhancement in strength may, on the one hand, result from improved B_4C filler dispersion due to the presence of CTAB, which reduces structural defects. More importantly, the observed strength enhancement is likely due to improved interfacial interactions between the matrix and B_4C particles, promoted by the presence of CTAB. Enhanced particle dispersion not only reduces interfacial defects but also enables the ultrahard B_4C particles to function as micro-reinforcements, analogous to microaggregates in concrete. This facilitates more uniform stress distribution throughout the composite and alleviates stress concentrations around the fillers. Ultimately, the strengthening mechanisms introduced by CTAB outweigh the adverse effects of increased porosity, leading to an overall improvement in mechanical performance.

Fig. 5(d) presents the X-ray diffraction (XRD) patterns of both the MK precursor and the geopolymer samples. The MK precursor exhibits a broad amorphous hump within the 2θ range of 15–30°, centered around 22°, along with minor crystalline peaks corresponding to anatase (TiO_2) and quartz (SiO_2). These crystalline phases remained inert in all alkali-activated samples. Following geopolymerisation, the broad hump shifts to a higher 2θ range of 20–35°, with a maximum around 29°, indicating a more disordered short-range structure compared to the original silicoaluminate precursor. Notably, the incorporation and increasing content of B_4C had no discernible impact on the amorphous structure of the geopolymer matrix. Nevertheless, the intensity of the characteristic crystalline peaks of B_4C increased proportionally with its content, suggesting that B_4C functions primarily as an inert filler within the geopolymer matrix.

3.4. Molecular-scale analysis via MAS NMR spectroscopy

3.4.1. ^{11}B MAS NMR

Fig. 6 presents the MAS NMR spectra of ^{11}B for all geopolymer samples containing B_4C. Previous studies have identified two distinct chemical environments for boron in B_4C compounds [56]. One arises from B_{12} icosahedra, associated with chemical shifts in the range of −5 to 0 ppm, where the boron atoms exhibit approximately sp^2 hybridisation and experience a deshielded, low electron density [57]. The second environment is primarily derived from C–B–C or B–B–C chains, corresponding to chemical shifts between 10 and 20 ppm, where boron atoms have nearly sp^3 hybridisation and reside in a more shielded, high electron density environment [58]. In the present study, the NMR spectra show broad resonance peaks centred at $\delta = -4$ ppm, indicating that most boron atoms in the B_4C used here were present in the more stable B_{12} icosahedral configuration. Notably, the spectral profiles of B in all samples remained unchanged compared to that of pure B_4C, except for variations in peak intensity proportional to B_4C content. This suggests that the introduced B_4C did not undergo chemical reaction during alkaline activation or subsequent geopolymerisation, and remained in the hardened samples primarily as an inert filler.

3.4.2. ^{27}Al MAS NMR

Fig. 7 presents the ^{27}Al MAS NMR spectra and corresponding deconvolution results for all samples investigated in this study, along with the MK precursor. In MK, aluminium existed predominantly as Al_4, Al_5, and Al_6 species, which appeared in the NMR spectra in order of increasing field strength, as is typical for natural aluminosilicate materials [59]. Following geopolymerisation (Fig. 7(b) and (c)), the signals corresponding to Al_5 and Al_6 diminished significantly, nearly disappearing, while the intensity of the Al_4 peak increased. This transformation reflected the dissolution of Al_5 and Al_6 species from MK into the alkaline activator, followed by their reprecipitation as Al_4 in the

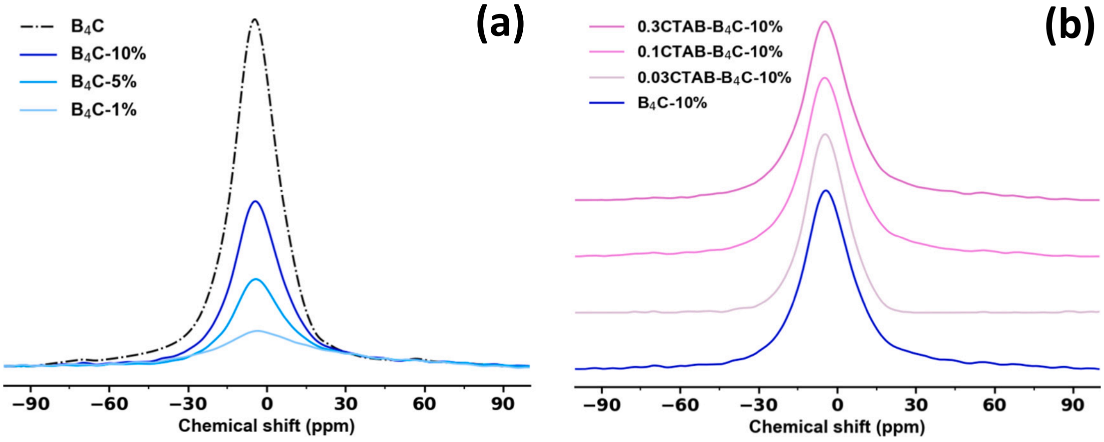

Fig. 6. ^{11}B MAS NMR spectra of (a) samples without CTAB but mixed with different levels of B_4C, (b) samples containing 10 wt% of B_4C but with different levels of CTAB.

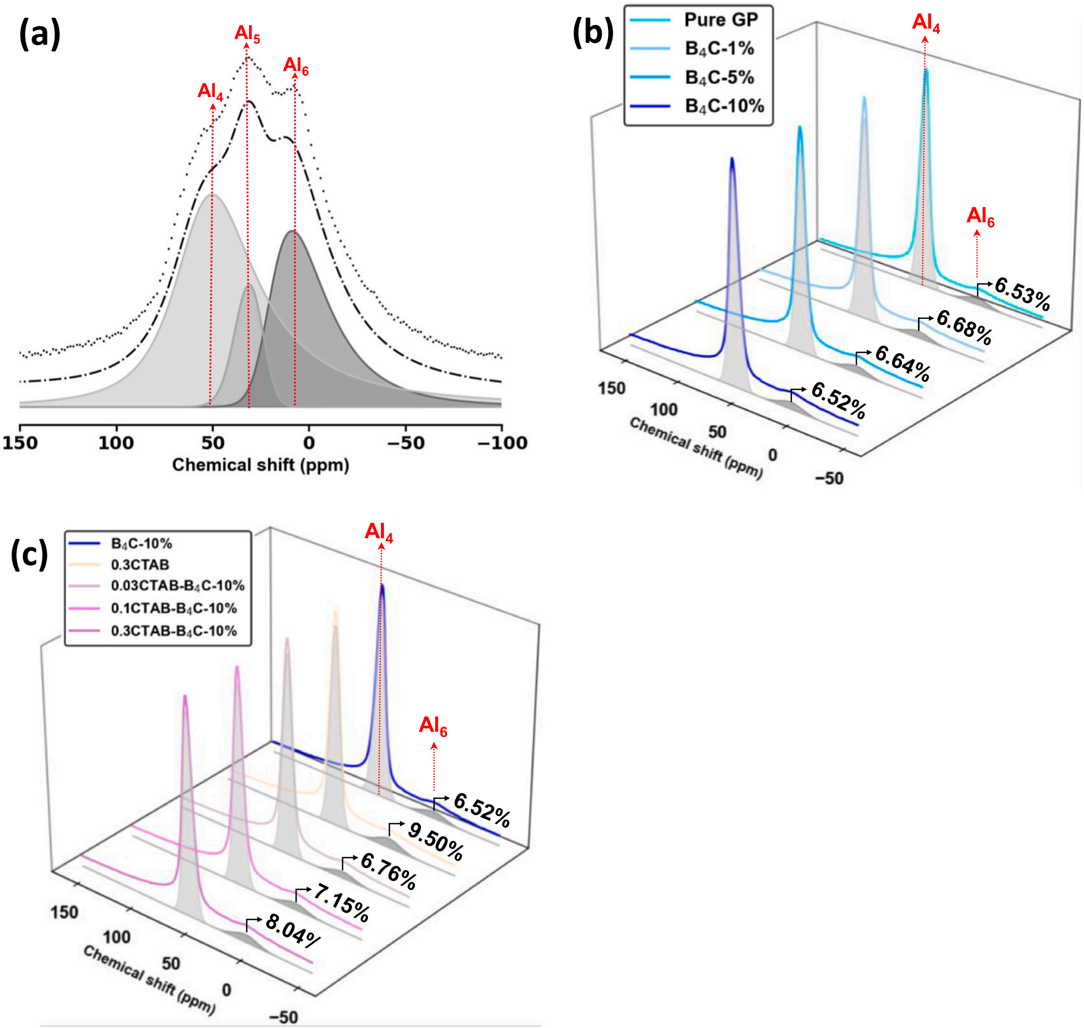

Fig. 7. ^{27}Al MAS NMR spectra (normalised to the highest spectral intensity) along with the molar distributions of Al coordination environments obtained through spectral deconvolution for (a) MK, (b) samples containing different B_4C contents, and (c) samples incorporating CTAB and B_4C.

formation of K-A-S-H gels. The residual Al_6 content in the final geopolymer matrix therefore served as an indicator of the extent of initial depolymerisation. As shown in Fig. 7(b), the addition of B_4C scarcely affected the Al_6 content, suggesting that B_4C had no influence on the early-stage depolymerisation of MK. Combined with the ^{11}B NMR results (Fig. 6), this implied that B_4C remained chemically inert, functioning as a passive filler within the matrix. In contrast, a different behaviour was observed in systems containing CTAB (Fig. 7(c)). Here, the Al_6 content increased with increasing CTAB dosage in the presence of 10 wt% B_4C, with a more pronounced effect observed in the absence of B_4C. This increase is attributed to CTAB aggregation around MK particles during the initial depolymerisation stage, which inhibited MK dissolution. However, in the presence of B_4C, part of the CTAB aggregated around the B_4C particles instead, partially mitigating its inhibitory effect on MK solubility. These observations aligned with the solubility assessment results shown in Fig. 2(b).

3.4.3. ^{29}Si MAS NMR

In aluminosilicate systems, including geopolymers, the Si structural environment is commonly described using the notation Q^n(mAl), where n represents the total number of tetrahedrally coordinated atoms connected to a given SiO_4 unit, and m specifies the number of aluminium atoms among them. Our previous studies have identified a variety of local Si environments in geopolymers, including Q^0, Q^1, Q^2(1Al), Q^3(1Al), Q^4(4Al), Q^4(3Al), Q^4(2Al), Q^4(1Al) and Q^4(0Al), which correspond to chemical shifts of approximately $\delta = -68 \pm 5$, -76 ± 5, -80 ± 3, -86 ± 4, -88 ± 3, -94 ± 4, -100 ± 5, -105 ± 4, and -115 ± 4 ppm, respectively [25,44]. In accordance with this principle, the ^{29}Si MAS NMR signals of all geopolymer samples in this study, as well as those of the MK precursor, were deconvoluted into their corresponding components, as shown in Fig. 8.

The ^{29}Si MAS NMR spectrum of MK and its deconvolution results are presented in Fig. 8(a). The Si structure in MK is primarily composed of Al-unsaturated Si tetrahedra (Q^4(mAl), where $m < 4$). In addition, a small amount of non-tetrahedral Si species (Q^n, $n < 4$) is also present. Following alkali activation and subsequent geopolymerisation (Fig. 8(b) and (c)), the content of Al-unsaturated Si tetrahedra—particularly low-Al units (Q^4(mAl), where $m < 2$)—decreased significantly. This corresponded to an increase in both high Al ($m = 3, 4$) tetrahedral Si units and non-tetrahedral Si species (Q^3). This transformation is attributed to extensive cleavage of Si–O–Si bonds during the dissolution and depolymerisation of MK in highly alkaline activators, resulting in the formation of free oligomeric Si species. During the subsequent polycondensation stage, some of these oligomeric units recombined with the framework to form network gels, leading to an increase in the content of polymeric Si units. Ultimately, the final Si environment in the geopolymer was dominated by Q^3 and high-Al ($m = 3, 4$) tetrahedral Q^4 units.

In the samples containing B_4C (Fig. 8(b)), the final chemical structure of Si appeared largely unaffected by either the presence or the

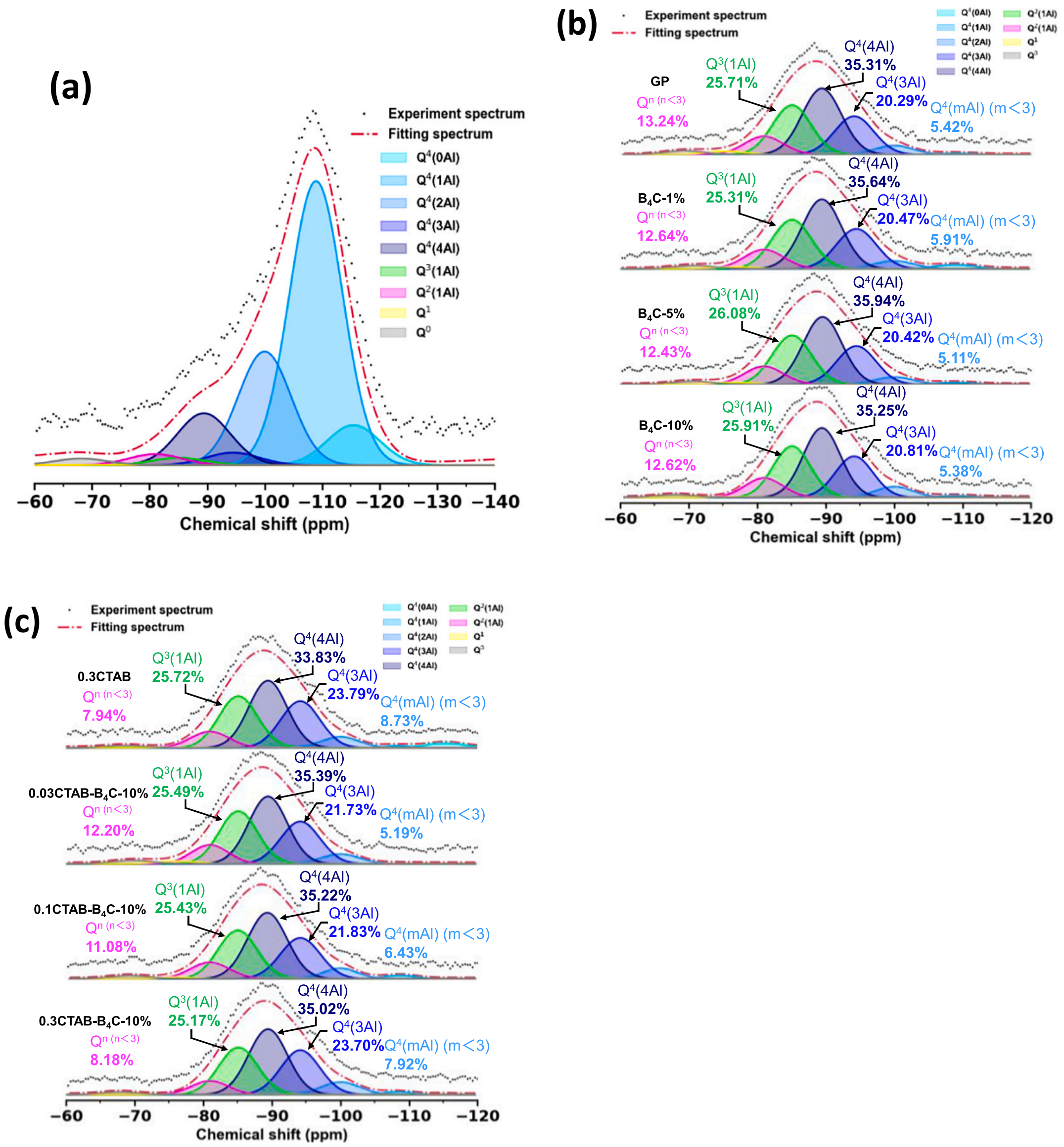

Fig. 8. Deconvolution analysis of ^{29}Si MAS NMR spectra and corresponding molar fractions of Si structural units (a) MK, (b) samples containing different B_4C contents, (c) samples incorporating CTAB and B_4C.

dosage of B_4C. This suggests that B_4C had minimal influence on the dissolution, depolymerisation, or subsequent polycondensation of Si species derived from MK. In contrast, in the samples with CTAB (Fig. 8 (c)), an increase in low-Al tetrahedral Si species (Q^4(mAl), $m < 3$), originating from the MK precursor, was accompanied by a decrease in oligomeric Si units (Q^n, $n < 3$). This indicates that CTAB partially inhibited the dissolution of MK, likely by adsorbing onto the surface of MK particles, thereby increasing the retention of low-Al tetrahedral Si species while reducing the formation of depolymerised oligomeric Si units. When CTAB was added to the B_4C-containing system, this inhibitory effect on MK dissolution was alleviated, presumably due to interactions between CTAB and B_4C. These observations are consistent with the ^{27}Al MAS NMR results (Fig. 7).

3.5. Micromorphology characteristics

Fig. 9 presents the micromorphological and elemental mapping images of samples containing 10 wt% B_4C and varying amounts of CTAB, as observed by EPMA. The elemental mapping reveals the enhanced concentrations of K, Si, and Al within approximately 30 μm of the B_4C particles with increasing CTAB content. This indicates a more extensive geopolymerisation in this region, characterised by the formation of continuous highly cross-linked Si–O–Si and Al–O–Si networks. The associated negative structural charges were likely balanced by K^+ ions. Furthermore, the reduced intensity of O from hydroxyl groups (e.g., Si–OH and Al–OH) also supports the notion that these groups were progressively converted into polymerised Si–O–Si and Al–O–Si linkages as the reaction proceeded. In addition, the decrease in O may also be attributed to CTAB aggregation, which reduced the local water content and consequently led to the formation of a denser gel structure. The enhanced geopolymerisation around the B_4C particles is primarily attributed to CTAB aggregation, which forms an interdigitated monolayer on the B_4C surface. This layer reverses the surface charge of the particle, facilitating the approach of OH^- anions to B_4C and creating a highly alkaline range that promotes the geopolymerisation of silica–aluminium species near the interface (Fig. 1b). Additionally, negatively charged silicate (SiO_4^{4-}), aluminate ($Al(OH)_4^-$), and other dissolved species from the MK will also tend to aggregate around the B_4C particles and deposit more rapidly, promoting the development of a dense, B_4C-core-based gel matrix.

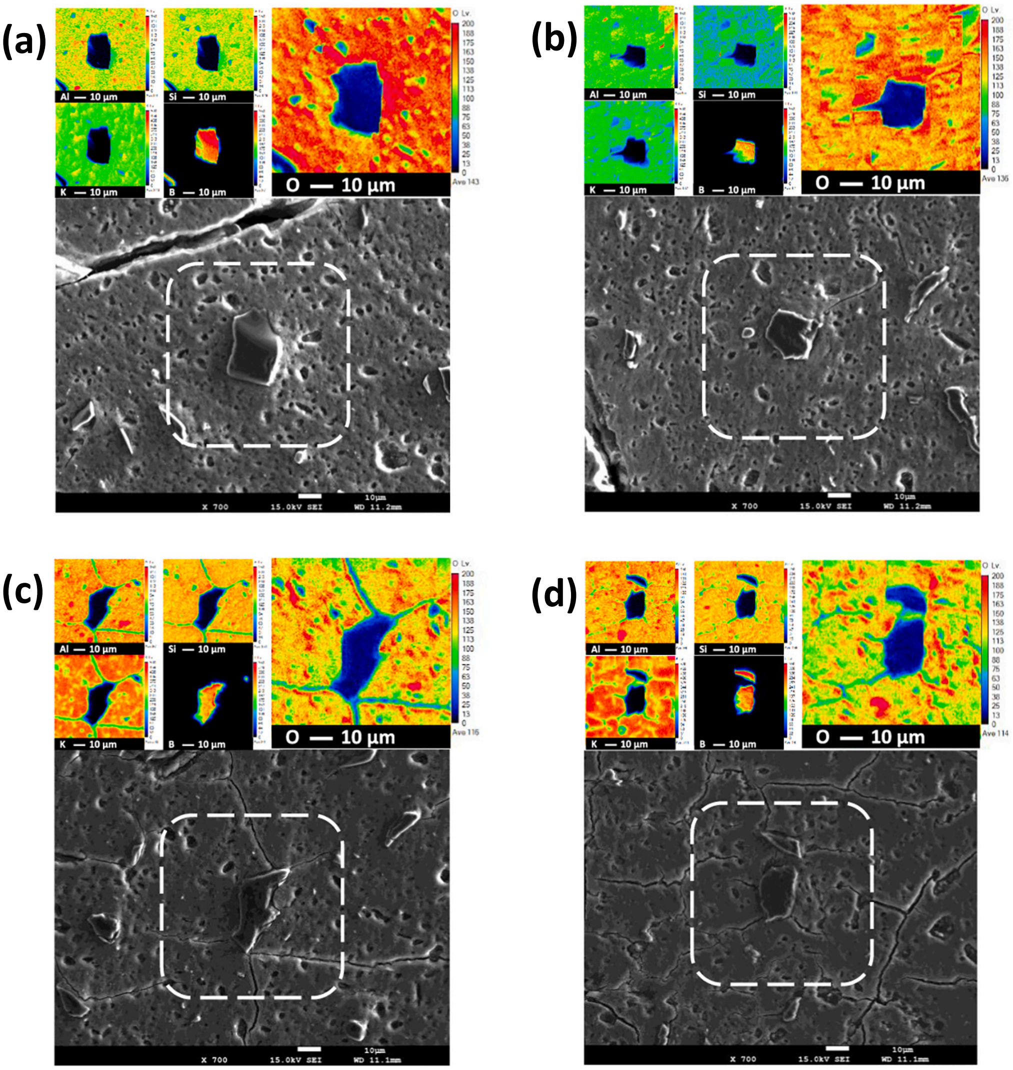

Fig. 9. Photomicrographs and elemental mapping images obtained by field emission-electron probe microanalysis (FE-EPMA) for (a) B_4C-10 %, (b) 0.03CTAB-B_4C-10 %, (c) 0.1CTAB-B_4C-10 %, (d) 0.3CTAB-B_4C-10 %.

From the SEI images below, it was observed that as the CTAB content increased, cracks progressively developed around the B_4C fillers embedded in the geopolymer matrix. This phenomenon may be explained by the fact that, although CTAB enhanced the degree of geopolymerisation around the B_4C particles—resulting in a denser matrix—the associated reduction in water content decreased internal flexibility, making the material more susceptible to drying-induced cracking, with the B_4C acting as a stress concentration centre. However, when considered alongside the compressive strength results, which showed an increase in strength with higher CTAB content (Fig. 5b), it was inferred that the cracks formed around the B_4C were primarily microcracks rather than through-thickness structural cracks. These microcracks tended to close under compressive loading and formed interlocking local stress fields with the filler, thereby having a negligible effect on the overall strength of the samples [60]. On the contrary, the enhanced matrix reactivity and the uniform distribution of microcracks contributed to the overall improvement in compressive strength.

To gain deeper insight into the structural characteristics of the interfacial transition zone (ITZ) between the B_4C filler and the geopolymer matrix, as well as to elucidate the mechanism underlying its transformation following the addition of CTAB, the micromorphology and elemental distribution at the nanoscale were systematically characterised, as shown in Fig. 10. The locations of the B_4C particles, the geopolymer matrix, and their interfacial contact regions were accurately identified according to selected area electron diffraction (SAED) and point energy-dispersive X-ray spectroscopy (EDS). In the system without CTAB, a 'weak shell layer' approximately 500 nm in thickness was observed at the interface between the B_4C particles and the geopolymer matrix as the ITZ, which was characterised by a loosely connected three-dimensional network and the presence of a visible gap between the particle surface and the matrix (Fig. 10(a)). Elemental mapping by STEM (Fig. 10(c)) further revealed that, despite similar Al/Si ratios, this region (Area #1) exhibited lower concentrations of both K and O compared to the more distant matrix (Area #2). In contrast, no loosely structured layer was observed near the B_4C surface in the CTAB-modified system. And the B_4C particles were more tightly embedded within the surrounding matrix, and no discernible interfacial gaps were present (Fig. 10(b)). Simultaneously, the interface exhibited a consistent structural morphology and Si/Al/O ratios. However, the region within approximately 2 µm of the B_4C surface contained a significant concentration of K (Fig. 10(d)), indicating the presence of a more extensive ITZ than previously identified.

Based on micromorphological and elemental composition analyses, the ITZs formed around B_4C particles in the geopolymer matrix were found to differ markedly depending on the presence or absence of CTAB. In systems without CTAB, although the unmodified B_4C particles carry a

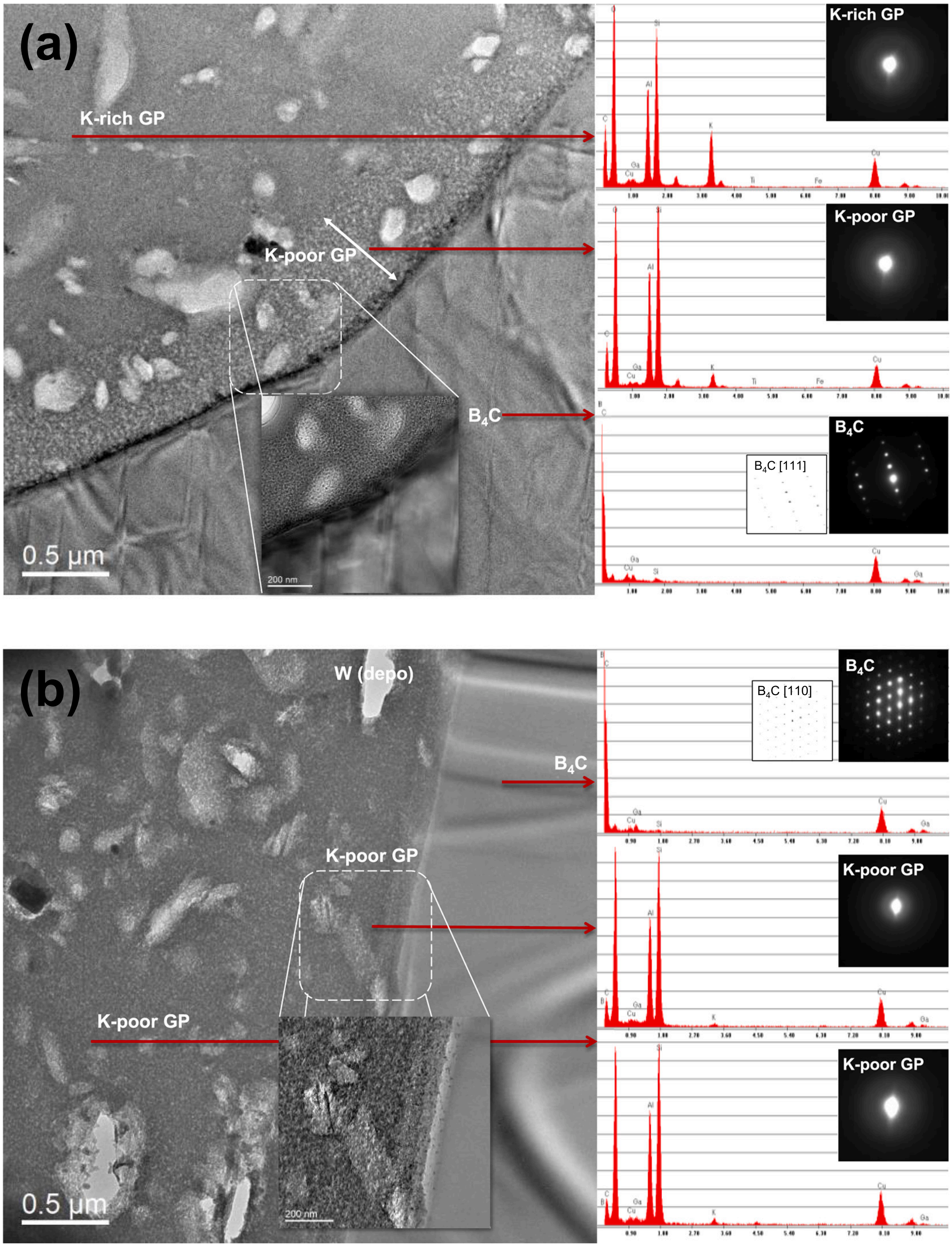

Fig. 10. TEM micrographs, selected area electron diffraction (SAED) and STEM-EDS point analysis of (a) B_4C-10 %, (b) 0.3CTAB-B_4C-10 % and STEM-EDS mapping analysis of (c) B_4C-10 %, (d) 0.3CTAB-B_4C-10 %.

negative surface charge and can attract K^+ ions to some extent, they exhibit a repulsive interaction with OH^- ions and free Si/Al monomers. Furthermore, the poor surface polarity of B_4C repels water molecules within a certain proximity, hindering the dissolution and diffusion of free Si and Al species and thus significantly limiting gel formation in this region. Consequently, a poorly gelled, weakly bonded transition zone (approximately 500 nm) develops, characterised by low structural integrity and a deficiency of K^+ ions, which fail to be efficiently incorporated due to their small ionic radius and high mobility compared to Al/Si monomer species. In contrast, in systems containing CTAB, the surfactant self-assembles on the B_4C surface to form a positively charged modification layer (Fig. 1), repelling K^+ ions away from the interface. However, the accumulation of OH^- ions and free Si/Al species, along with abundant $CTAB^+$ capable of charge compensation, promotes the formation of a K^+-deficient but highly crosslinked CTAB-A-S-H gel. This gel encapsulates the B_4C particles tightly, contributing to enhanced structural integrity and overall mechanical strength of the composite (Fig. 5).

It should be emphasised that the proposed mechanism for the formation of a K^+-deficient interfacial gel around B_4C particles—particularly in the absence of CTAB—remains hypothetical at this stage. Although it is based on micromorphological observations and the

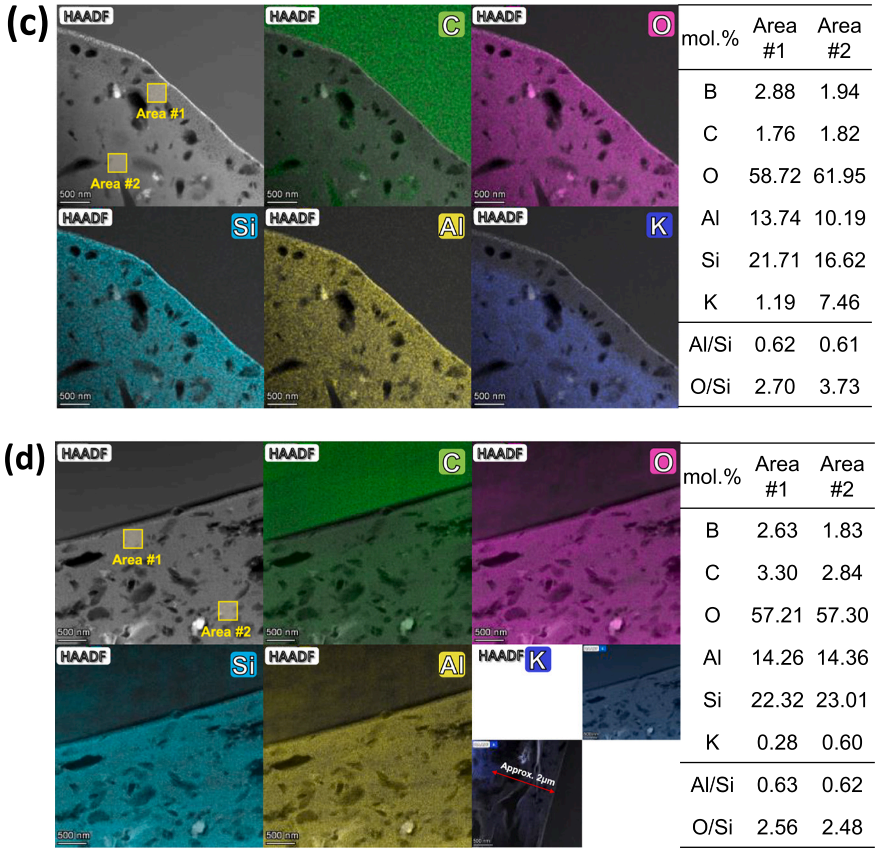

(c)

mol.%	Area #1	Area #2
B	2.88	1.94
C	1.76	1.82
O	58.72	61.95
Al	13.74	10.19
Si	21.71	16.62
K	1.19	7.46
Al/Si	0.62	0.61
O/Si	2.70	3.73

(d)

mol.%	Area #1	Area #2
B	2.63	1.83
C	3.30	2.84
O	57.21	57.30
Al	14.26	14.36
Si	22.32	23.01
K	0.28	0.60
Al/Si	0.63	0.62
O/Si	2.56	2.48

Fig. 10. (*continued*).

surface electrostatic characteristics revealed in this study (e.g., Fig. 1), there is currently a lack of direct experimental evidence or precedent in the existing literature that confirms such localised ionic segregation or gel deficiency at the B_4C–geopolymer interface. To verify this interfacial mechanism, further investigations using spatially resolved analytical techniques are required. Potential approaches may include solid-state

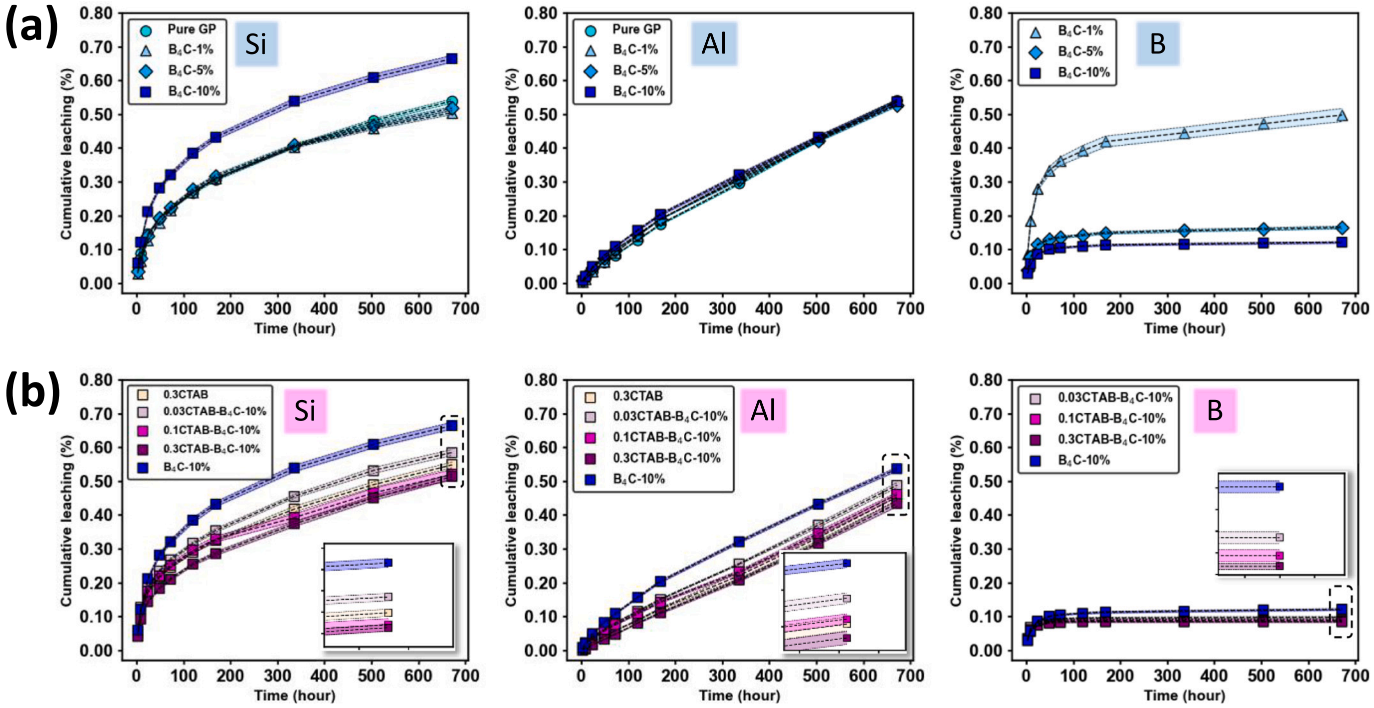

Fig. 11. Cumulative leaching fractions of Si, Al, and B from dynamic leaching tests for (a) samples without CTAB and (b) samples with CTAB. Shaded colour bands represent the envelopes defined by the minimum and maximum values from triplicate measurements at each time point.

NMR for identifying chemical environments of K^+, Al, and Si species, and nano-FTIR or Raman mapping to probe the crosslinking density and gel composition at the sub-micron scale. These methods could help determine whether such a K^+-deficient, weakly polymerised transition zone indeed forms in the absence of CTAB.

3.6. *Stability in aqueous environments*

The chemical stability of geopolymers as shielding materials for radioactive wasteforms was evaluated under simulated near-field groundwater conditions through leaching experiments. Fig. 11 presents the leaching results for all samples in the laboratory-simulated aqueous environment, focusing on the structural elements Si and Al, as well as B, which was introduced as a neutron absorber. Fig. 11(a) presents the results of leaching experiments on geopolymer samples without CTAB, incorporating varying amounts of B_4C. At low levels of B_4C addition, the cumulative leaching fraction of Si remained largely unchanged compared to the pure geopolymer, reaching approximately 0.5 % after 28 days. However, when the B_4C content increased to 10 wt %, Si leaching rose slightly, reaching around 0.7 %. In contrast to the behaviour of Si, Al leaching remained largely unaffected by the amount of B_4C added, maintaining a cumulative fraction of approximately 0.55 % over the same period. This discrepancy in leaching behaviour of Si and Al is primarily attributed to differences in the molecular size of the respective species in the geopolymer matrix. It is widely accepted that the leached species of Si and Al originate from incompletely geopolymerised frameworks and unreacted aluminosilicate precursors, released as $Si(OH)_4$ monomers (< 0.4 nm) or oligomers ($> > 1$ nm) and as solvated aluminate ions $[Al(OH)_4]^-$ (< 0.4 nm), respectively [61–63]. Although B_4C addition exerted minimal influence on the geopolymerisation process and the chemical composition of matrix, gravitational settling and electrostatic repulsion (Fig. 5) led to uneven B_4C distribution and the formation of porous interfacial transition zones (ITZs) between filler and matrix (Fig. 10), increasing the structural looseness. At low B_4C levels, this enhanced looseness exerted little influence on the mobility of small $Si(OH)_4$ species. However, at higher B_4C contents (10 wt%), larger Si oligomers could also migrate through the matrix, leading to increased overall Si leaching. In comparison, the smaller $[Al(OH)_4]^-$ ions readily diffused even within a compact matrix, rendering further loosening ineffective in enhancing Al leaching. Interestingly, B leaching decreased apparently with increasing B_4C content. This phenomenon stems from the fact that B leaching is primarily governed by the effective surface area of B_4C particles exposed to the leaching solution. Although samples with higher B_4C contents contain more B_4C overall, much of it remained embedded within the matrix and was not directly accessible to the leaching medium. As a result, the actual amount of B leached remained relatively constant across all B_4C-containing sample, while the increase in the initial total B content led to a marked decrease in the cumulative leaching fraction.

Fig. 11(b) presents the leaching behaviour of samples containing 10 wt% B_4C with varying CTAB concentrations, alongside a control sample with a CTAB index of 30 but without B_4C. The results indicate that the cumulative leaching fraction of Si progressively decreased with increasing CTAB content. Notably, at the highest CTAB level, the Si leaching was lower than that of the B_4C-free control. A similar trend was observed for Al, with leaching fractions decreasing as CTAB content increased; the sample with the highest CTAB index also exhibited lower Al leaching than the control. This reduction in Si and Al leaching can be attributed to two main factors. First, the addition of CTAB enhances the densification of the geopolymer matrix, particularly improving the structure of the interfacial transition zone (ITZ) between the matrix and the B_4C filler, as evidenced in Figs. 9 and 10. Second, the positively charged CTAB molecules may electrostatically attract free monomeric anions in the matrix, thereby reducing their mobility and dissolution. In the absence of B_4C, although CTAB was still present, the lack of adsorption or interaction with B_4C may have led to an excess of CTAB. This surplus could inhibit the geopolymerisation process, resulting in an increased concentration of free monomeric anions not incorporated into the matrix structure, and thus elevated leaching of Si and Al. These findings further confirm the strong synergistic effect between B_4C and CTAB during geopolymerisation, as supported by the earlier chemical deformation analysis (Fig. 4) and NMR results (Figs. 7 and 8). Additionally, a slight reduction in B leaching was observed upon CTAB addition, suggesting that CTAB may inhibit B dissolution by self-assembling a surface coating on B_4C particles.

3.7. *Evaluation of neutron shielding performance*

The neutron transmission results presented in Fig. 12 highlight the variation in neutron shielding performance of the samples under different conditions. As shown in the transmission luminance image in Fig. 12(a), geopolymer samples without B_4C exhibited higher brightness at thinner thicknesses (especially at 10 mm), indicating poor neutron shielding capability. In contrast, samples with B_4C at the same thickness showed significantly lower luminance, reflecting enhanced neutron absorption. As the sample thickness increased, the overall luminance of all transmission images decreased, regardless of B_4C inclusion, suggesting that the geopolymer matrix possessed some intrinsic neutron shielding capacity, which improved with greater thickness. Additionally, the use of paraffin during demolding appeared to have no significant effect on neutron shielding performance.

Fig. 12(b) shows grayscale profiles along selected scan lines for the 10 mm and 20 mm samples—the only thicknesses that exhibited measurable neutron transmission under the test conditions. Thicker samples transmitted too little neutron intensity to yield discernible grayscale variations, resulting in uniformly dark images. Thus, quantitative analysis was limited to the 10 mm and 20 mm specimens, where transmission remained comparable. At 10 mm, the incorporation of B_4C reduced neutron transmittance by more than 80 %, clearly demonstrating its strong shielding effectiveness. Even at 20 mm, where B_4C-free samples already exhibited substantial attenuation, the addition of B_4C further enhanced shielding performance, as reflected by a more pronounced decrease in grayscale intensity. In an ideal case, a sample with a perfectly homogeneous internal structure and composition would yield a flat grayscale profile across the horizontal axis of the neutron transmission image, indicating uniform neutron attenuation throughout the cross-section. However, in practice, phenomena such as diffraction, scattering, beam divergence, and flux distribution variations can influence the measured grayscale profile [64]. These effects may lead to slight spatial variations in neutron intensity across the sample, which are inherent to the imaging technique rather than the material itself. In unmodified geopolymers, the absence of elements with high neutron absorption cross-sections led to relatively weak and uniform neutron attenuation throughout the material. This suggests a homogeneous distribution of elements within the geopolymer matrix, with no discrete regions exhibiting enhanced neutron absorption. In contrast, the incorporation of B_4C (10 wt% of MK), facilitated by CTAB (30 wt% of B_4C) dispersion and comprising boron with a high neutron absorption cross-section, significantly improved the overall shielding performance. The greater attenuation was uniformly distributed across the entire cross-section, rather than being localised. This indicates that the modified geopolymer, under this design strategy, provides effective and uniform neutron radiation shielding.

4. Conclusions

In this study, the use of B_4C as a functional filler, assisted by CTAB as a dispersant and stabiliser, successfully enhanced the neutron shielding capability of metakaolin-based geopolymers while preserving reasonable mechanical strength and environmental durability. The key findings are as follows:

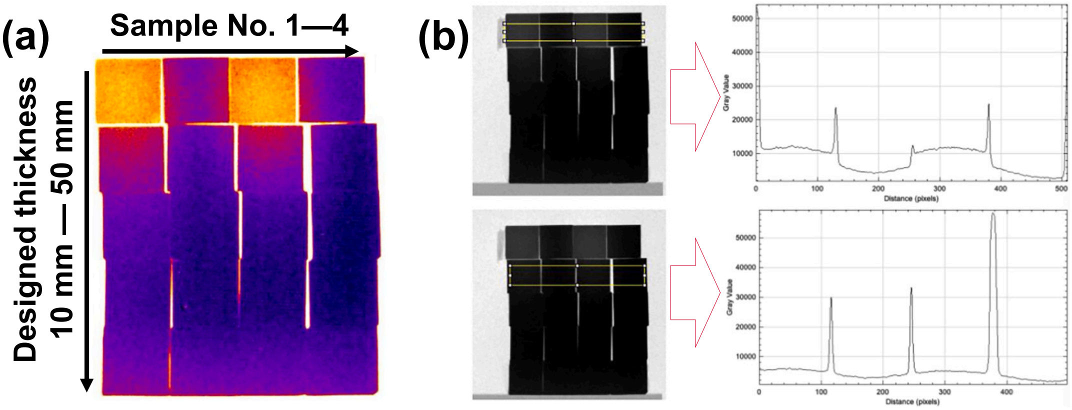

Fig. 12. (a) Neutron transmission brightness image of geopolymer samples (No.1–4) acquired using the nFPD. No.1: B_4C/CTAB-free, wax-coated demoulding; No.2: B_4C/CTAB-added, wax-coated demoulding; No.3: B_4C/CTAB-free, air-dried demoulding; No.4: B_4C/CTAB-added, air-dried demoulding. Brighter areas indicate higher neutron transmission and thus lower shielding performance. (b) Grey value profiles extracted along the central horizontal line in (a), showing the spatial distribution of neutron transmittance across each sample.

1) CTAB-modified B_4C particles exhibit enhanced dispersion and interfacial bonding within the geopolymer matrix, resulting from a reversal in surface charge from negative to positive. This charge adjustment promotes a uniform distribution and reduces CTAB's inhibitory effect on metakaolin dissolution. Electrostatic interactions between B_4C and CTAB contribute to matrix densification and mechanical reinforcement.
2) The incorporation of B_4C improves flowability and extends the setting time of fresh paste without causing noticeable changes in gel chemistry or measurable volumetric instability during the monitoring period. However, it reduces mechanical strength due to weak bonding at the filler–matrix interface. CTAB enhances particle dispersion and delays setting, though it slightly increases unreacted precursors and porosity. Nevertheless, the synergistic action of B_4C and CTAB improves filler distribution and stress transfer, ultimately restoring mechanical performance.
3) Microstructural analysis reveals distinct interfacial transition zones (ITZs) between B_4C and the geopolymer matrix. Without CTAB, the negatively charged, weakly polar B_4C surfaces hinder gelation, forming porous, K-deficient ITZs with poor bonding. With CTAB, positively charged surfaces attract OH^- and promote Si/Al aggregation, forming a dense, K-enriched network. However, near the particle, CTAB forms a positive barrier that repels K^+ but stabilises a compact, K-deficient ITZ, tightly encapsulating B_4C and enhancing strength.
4) The resulting geopolymers demonstrate good chemical stability in aqueous environments. At low B_4C contents, elemental leaching remains minimal. At higher loadings, Si leaching slightly increases due to a more porous ITZ, while Al largely remains unaffected. B leaching depends on surface exposure. CTAB improves Si and Al retention by densifying the ITZ and inhibiting B dissolution. Neutron imaging verifies enhanced and uniform shielding performance resulting from CTAB-assisted B_4C incorporation.

CRediT authorship contribution statement

Xiaobo Niu: Writing – review & editing, Writing – original draft, Visualization, Validation, Methodology, Investigation, Formal analysis, Data curation, Conceptualization. **Yogarajah Elakneswaran:** Writing – review & editing, Supervision, Project administration, Methodology, Funding acquisition, Formal analysis, Conceptualization. **Ryosuke Kikuchi:** Writing – review & editing, Methodology, Investigation, Data curation. **Ang Li:** Writing – review & editing, Formal analysis, Data curation. **Sivasubramaniam Seralathan:** Writing – review & editing, Data curation. **Yoshihisa Hiraki:** Writing – review & editing, Supervision, Methodology, Conceptualization. **Junya Sato:** Writing – review & editing, Supervision, Methodology, Conceptualization. **Takeshi Osugi:** Writing – review & editing, Supervision, Methodology, Conceptualization. **Takashi Kamiyama:** Writing – review & editing, Resources, Methodology, Conceptualization. **Brant Walkley:** Writing – review & editing, Supervision, Methodology, Funding acquisition, Conceptualization.

Declaration of competing interest

The authors declare that they have no known competing financial interests or personal relationships that could have appeared to influence the work reported in this paper.

Data availability

Data will be made available on request.

Acknowledgements

This work was partially supported by the JAEA Nuclear Energy Science & Technology and Human Resource Development Project (Grant No. JPJA20P12345678), as well as by the UK EPSRC through grants EP/Y029208/1 and EP/T013524/1. We gratefully acknowledge the Instrumental Analysis Support Office at the Frontier Chemistry Center, Faculty of Engineering, Hokkaido University, for granting access to the Solid 500 MHz (BRUKER) NMR and for their valuable technical support and expertise. We would like to express our sincere gratitude to Dr. Ken Fujiwara of the National Institute of Advanced Industrial Science and Technology (AIST) for his invaluable assistance in the neutron transmission experiments.

Appendix A. Supplementary data

Supplementary data to this article can be found online at https://doi.org/10.1016/j.cemconres.2025.108096.

References

[1] TEPCO, Basic Policy for the Contaminated Water Issue at the TEPCO's Fukushima Daiichi Nuclear Power Station. https://www.mofa.go.jp/policy/page3e_000072.html, 2013.

[2] R. Gauntt, D. Kalinich, J. Cardoni, J. Phillips, A. Goldmann, S. Pickering, M. Francis, K. Robb, L. Ott, D. Wang, C. Smith, S. St. Germain, D. Schwieder, C. Phelan, Fukushima Daiichi Accident Study (Status as of April 2012), Sandia Report 6173 (2012), https://doi.org/10.2172/1055601.

[3] H. Takuma, Y. Isao, N. Ryuji, K. Ryunosuke, Preparation of carbonate slurry simulating chemical composition of slurry in overflowed high integrity container and evaluation of its characteristics, JAEA Technol. 012 (2021), https://doi.org/10.11484/jaea-technology-2021-012.

[4] G. Steinhauser, Fukushima's forgotten radionuclides: a review of the understudied radioactive emissions, Environ. Sci. Technol. 48 (2014) 4649–4663, https://doi.org/10.1021/es405654c.

[5] Z. Zhang, K. Ninomiya, Y. Yamaguchi, K. Kita, H. Tsuruta, Y. Igarashi, A. Shinohara, Atmospheric activity concentration of ^{90}Sr and ^{137}Cs after the fukushima daiichi nuclear accident, Sci. Technol. 53 (2018) 9917–9925, https://doi.org/10.1021/acs.est.8b01697.

[6] X. Li, R. Selesnick, Q. Schiller, K. Zhang, H. Zhao, D.N. Baker, M.A. Temerin, Measurement of electrons from albedo neutron decay and neutron density in near-Earth space, Nature 553 (2017) 382–385, https://doi.org/10.1038/nature24642.

[7] A. Pietropaolo, The physical mechanisms of neutron detection, Contemp. Phys. 64 (2023) 194–223, https://doi.org/10.1080/00107514.2024.2314817.

[8] K. Kamiya, K. Ozasa, S. Akiba, O. Niwa, K. Kodama, N. Takamura, E.K. Zaharieva, Y. Kimura, R. Wakeford, Long-term effects of radiation exposure on health, Lancet 386 (2015) 469–478, https://doi.org/10.1016/S0140-6736(15)61167-9.

[9] D.L. Stricklin, J. VanHorne-Sealy, C.I. Rios, L.A.S. Carnell, L.P. Taliaferro, Neutron radiobiology and dosimetry, Radiat. Res. 195 (2021) 480–496, https://doi.org/10.1667/RADE-20-00213.1.

[10] V. Tran, M.P. Little, Dose and dose rate extrapolation factors for malignant and non-malignant health endpoints after exposure to gamma and neutron radiation, Radiat. Environ. Biophys. 56 (2017) 299–328, https://doi.org/10.1007/s00411-017-0707-4.

[11] A. Hasegawa, K. Tanigawa, A. Ohtsuru, H. Yabe, M. Maeda, J. Shigemura, T. Ohira, T. Tominaga, M. Akashi, N. Hirohashi, T. Ishikawa, K. Kamiya, K. Shibuya, S. Yamashita, R.K. Chhem, Health effects of radiation and other health problems in the aftermath of nuclear accidents, with an emphasis on Fukushima, Lancet 386 (2015) 479–488, https://doi.org/10.1016/S0140-6736(15)61169-9.

[12] E. Gallego, A. Lorente, H.R. Vega-Carrillo, Testing of a high-density concrete as neutron shielding material, Nucl. Technol. 168 (2009) 399–404, https://doi.org/10.13182/NT09-A9216.

[13] X. Zhang, M. Yang, X. Zhang, H. Wu, S. Guo, Y. Wang, Enhancing the neutron shielding ability of polyethylene composites with an alternating multi-layered structure, Compos. Sci. Technol. 150 (2017) 16–23, https://doi.org/10.1016/j.compscitech.2017.06.007.

[14] Y. Zhou, X. Chen, Y. Zhan, S. Wang, J. Xu, Review of the transmittance effects and long-term radiation mechanisms of γ on heavy concrete, Prog. Nucl. Energy 175 (2024) 105353, https://doi.org/10.1016/j.pnucene.2024.105353.

[15] M.A. Khalaf, C.C. Ban, M. Ramli, The constituents, properties and application of heavyweight concrete: a review, Construct. Build Mater. 215 (2019) 73–89, https://doi.org/10.1016/j.conbuildmat.2019.04.146.

[16] R.L. Clough, High-energy radiation and polymers: a review of commercial processes and emerging applications, Nucl. Instrum. Methods Phys. Res. Sect. B 185 (2001) 1–4, https://doi.org/10.1016/S0168-583X(01)00966-1.

[17] X. Niu, Y. Elakneswaran, R.I. Chaerun, J.L. Provis, T. Sato, Adsorption behaviour of simulant radionuclide cations and anions in metakaolin-based geopolymer, J. Hazard. Mater. 429 (2022) 128373, https://doi.org/10.1016/j.jhazmat.2022.128373.

[18] R.I. Chaerun, N. Soonthornwiphat, K. Toda, K. Kuroda, X. Niu, R. Kikuchi, T. Otake, Y. Elakneswaran, J.L. Provis, T. Sato, Retention mechanism of cesium in chabazite embedded into metakaolin-based alkali activated materials, J. Hazard. Mater. 440 (2022) 129732, https://doi.org/10.1016/j.jhazmat.2022.129732.

[19] D.A. Geddes, M.C. Stennett, T.J. Wilkinson, B.E. Griffith, J.V. Hanna, J.L. Provis, B. Walkley, Alkali-mediated Sr incorporation mechanism and binding capacity of alkali aluminosilicate hydrate in geopolymers, J. Hazard. Mater. 488 (2025) 137246, https://doi.org/10.1016/j.jhazmat.2025.137426.

[20] X. Niu, Y. Elakneswaran, R.I. Chaerun, C. Fang, J.L. Provis, T. Sato, Development of metakaolin-based geopolymer for selenium oxyanions uptake through in-situ ettringite formation, Sep. Purif. Technol. 324 (2023) 124530, https://doi.org/10.1016/j.seppur.2023.124530.

[21] D.P. Mitchell, The absorption of neutrons detected by boron and lithium, Phys. Rev. 49 (1936) 453–458, https://doi.org/10.1103/PhysRev.49.453.

[22] R. Vaghetto, M. Childs, E. Kee, Y.A. Hassan, Observations and measurements of boric acid precipitation scenarios, Prog. Nucl. Energy 91 (2016) 302–309, https://doi.org/10.1016/j.pnucene.2016.05.011.

[23] W. Zhang, T. Liu, J. Xu, Preparation and characterisation of ^{10}B boric acid with high purity for nuclear industry, SpringerPlus 5 (2016) 1202, https://doi.org/10.1186/s40064-016-2310-6.

[24] H. Guo, P. Sciora, T. Kooyman, L. Buiron, G. Rimpault, Application of boron carbide as burnable poison in sodium fast reactors, Nucl. Technol. 205 (2019) 1433–1446, https://doi.org/10.1080/00295450.2019.1620054.

[25] X. Niu, Y. Elakneswaran, A. Li, S. Seralathan, R. Kikuchi, Y. Hiraki, J. Sato, T. Osugi, B. Walkley, Incorporation of boron into metakaolin-based geopolymers for radionuclide immobilisation and neutron capture potential, Cem. Concr. Res. 190 (2025) 107814, https://doi.org/10.1016/j.cemconres.2025.107814.

[26] S.E. Chidiac, M.G. El-Samrah, M.A. Reda, M.A.E. Abdel-Rahman, Mechanical and radiation shielding properties of concrete containing commercial boron carbide powder, Construct. Build Mater. 313 (2021) 125466, https://doi.org/10.1016/j.conbuildmat.2021.125466.

[27] C. Zhu, G. Li, J. Wang, S. Dong, K. Cao, Y. Lv, Performance improvement in neutron-shielding ultra-high performance mortar prepared with alkaline-treated boron carbide, J. Build. Eng. 71 (2023) 106435, https://doi.org/10.1016/j.jobe.2023.106435.

[28] E. Phillip, T.F. Choo, N.W.A. Khairuddin, R.O.A. Rahman, On the sustainable utilization of geopolymers for safe management of radioactive waste: a review, Sustainability 15 (2023) 1117, https://doi.org/10.3390/su15021117.

[29] K. Nishikawa, S. Hashimoto, S. Rossignol, Fabrication of B$_4$C hardened body using geopolymer binder with cold reaction sintering and application to neutron shielding, Ceram. Int. 49 (2023) 12750–12757, https://doi.org/10.1016/j.ceramint.2022.12.140.

[30] A. Gadkar, K.V.L. Subramaniam, An evaluation of yield and Maxwell fluid behaviors of fly ash suspensions in alkali-silicate solutions, Mater. Struct. 52 (2019) 117, https://doi.org/10.1617/s11527-019-1429-7.

[31] L. Hou, J. Li, Z. Lu, Y. Niu, Influence of foaming agent on cement and foam concrete, Construct. Build Mater. 280 (2021) 122399, https://doi.org/10.1016/j.conbuildmat.2021.122399.

[32] J. Liu, J. Fu, Y. Yang, C. Gu, Study on dispersion, mechanical and microstructure properties of cement paste incorporating graphene sheets, Construct. Build Mater. 199 (2019) 1–11, https://doi.org/10.1016/j.conbuildmat.2018.12.006.

[33] A. Singhal, B.P. Gangwar, G. J.M., CTAB modified large surface area nanoporous geopolymer with high adsorption capacity for copper ion removal, Appl. Clay Sci. 150 (2017) 106–144, https://doi.org/10.1016/j.clay.2017.09.013.

[34] X. Yue, C. Cheng, A. Fan, J. Wang, K. Du, M. Jiang, No AccessEvaluation of the surfactant effect on the mechanical and pore properties of porous geopolymers, Green Mater. (2025), https://doi.org/10.1680/jgrma.24.00186.

[35] Z. Wang, D. Lu, Study on the effect of emulsifiers on the pore structures of geopolymer prepared by emulsion templating, Mater. Res. Express 7 (2020) 055508, https://doi.org/10.1088/2053-1591/ab94f9.

[36] Ö. Açışlı, İl. Acar, A. Khataee, Preparation of a surface modified fly ash-based geopolymer for removal of an anionic dye: parameters and adsorption mechanism, Chemosphere 295 (2022) 133870, https://doi.org/10.1016/j.chemosphere.2022.133870.

[37] H. Jin, K. Hong, J. Liu, C. Qiu, M. Zhu, C. Li, Q. Wang, Structural and functional design of CTAB-geopolymer adsorbents for rapid removal of tetracycline: a comparative study, Sep. Purif. Technol. 356 (2025) 129871, https://doi.org/10.1016/j.seppur.2024.129872.

[38] Architectural Institute of Japan, JASS 15M-103: Standard specifications for self-leveling materials, Architectural Institute of Japan, 2021.

[39] Standard test method for chemical shrinkage of hydraulic cement paste. West Conshohocken: American Society for Testing and Materials, ASTM C 1608 (2007).

[40] Janpanese Industrial Standard, Method of test for compressive strength of concrete, JIS A 1108 (2018) 1–5.

[41] R.M. Mironenko, O.B. Belskaya, V.P. Talsi, V.A. Likholobov, Quadrupolar magic angle spinning NMR spectra fitted using the Pearson IV function, Solid State Nucl. Magn. Reson. 63–64 (2014) 37–41, https://doi.org/10.1016/j.ssnmr.2014.10.001.

[42] American Nuclear Society, Measurement of the leachability of solidified low-level radioactive wastes by short-term test procedure. ANSI/ANS-16.1-2003, American Nuclear Society, Illinois, 2004, pp. 1–33.

[43] Y. Li, T. Qiu, Oxidation behaviour of boron carbide powder, Mater. Sci. Eng. A 444 (2007) 184–191, https://doi.org/10.1016/j.msea.2006.08.068.

[44] X. Niu, Y. Elakneswaran, Naoki Hiroyoshi, Surface chemistry and radionuclide anion immobilisation potential of phosphoric acid-activated metakaolin-based geopolymers, Cem. Concr. Res. 181 (2024) 107549, https://doi.org/10.1016/j.cemconres.2024.107549.

[45] V.K. Sharma, S. Mitra, V. Garcia Sakai, P.A. Hassan, J. Peter Embsd, R. Mukhopadhyay, The dynamical landscape in CTAB micelles, Soft Matter 8 (2012) 151–7160, https://doi.org/10.1039/C2SM25515D.

[46] D.D. Rodrigues, J.G. Broughton, Surface modification of boron carbide for improved adhesion to an epoxy matrix, in: V. Mittal (Ed.), Surface Modification of Nanoparticle and Natural Fiber Fillers Chapter2, Wiley, 2015, https://doi.org/10.1002/9783527670260.ch2.

[47] W. Meng, E. Gall, F. Ke, Z. Zeng, B. Kopchick, R. Timsina, X. Qiu, Structure and interaction of graphene oxide– cetyltrimethylammonium bromide complexation, J. Phys. Chem. 119 (2015) 21135–21140, https://doi.org/10.1021/acs.jpcc.5b04102.

[48] S. Kalam, S.A. Abu-Khamsin, M.S. Kamal, S. Patil, Surfactant adsorption isotherms: a review, ACS Omega 6 (2021) 32342–32348, https://doi.org/10.1021/acsomega.1c04661.

[49] N. Granizo, A. Palomo, A. Fernandez-Jiménez, Effect of temperature and alkaline concentration on metakaolin leaching kinetics, Ceram. Int. 40 (2014) 8975–8985, https://doi.org/10.1016/j.ceramint.2014.02.071.

[50] C.A. Rees, J.L. Provis, G.C. Lukey, J.S.J. van Deventer, The mechanism of geopolymer gel formation investigated through seeded nucleation, Colloids Surf. A Physicochem. Eng. Asp. 318 (2008) 1–3, https://doi.org/10.1016/j.colsurfa.2007.12.019.

[51] J. Sun, P. Zhang, Effects of different composite mineral admixtures on the early hydration and long-term properties of cement-based materials: a comparative study, Construct. Build Mater. 294 (2021) 123547, https://doi.org/10.1016/j.conbuildmat.2021.123547.

[52] Z. Li, S. Zhang, Y. Zuo, W. Chen, G. Ye, Chemical deformation of metakaolin based geopolymer, Cem. Concr. Res. 120 (2019) 108–118, https://doi.org/10.1016/j.cemconres.2019.03.017.

[53] X. Ke, V.A. Baki, Assessing the suitability of alkali-activated metakaolin geopolymer for thermochemical heat storage, Microporous Mesoporous Mater. 325 (2021) 111329, https://doi.org/10.1016/j.micromeso.2021.111329.

[54] A. Mohammadi, E. Ghiasvand, M. Nili, Relation between mechanical properties of concrete and alkali-silica reaction (ASR); a review, Construct. Build Mater. 258 (2020) 119567, https://doi.org/10.1016/j.conbuildmat.2020.119567.

[55] J. Tan, B. Sun, Z. Li, Superabsorbent polymer in alkali-activated slag paste: swelling-deswelling behaviour and effects on surrounding matrix, Cem. Concr. Compos. 146 (2024) 105365, https://doi.org/10.1016/j.cemconcomp.2023.105365.
[56] A.R. Siedle, Boron-11 NMR spectroscopy, Annu. Rep. NMR Spectrosc. 12 (1982) 177–261, https://doi.org/10.1016/S0066-4103(08)60218-5.
[57] D.R. Armstrong, P.G. Perkins, Calculation of ^{11}B chemical shifts in mixed halides of boron, Chem. Commun. (London) 15 (1965) 337–338, https://doi.org/10.1039/C19650000337.
[58] N. Vast, J. Sjakste, E. Betranhandy, Boron carbides from first principles, J. Phys. Conf. Ser. 176 (2009) 012002, https://doi.org/10.1088/1742-6596/176/1/012002.
[59] F. Taulelle, B. Bouchevreaua, C. Martineaua, NMR crystallography driven structure determination: nanoporous materials, Cryst. Eng. Comm. 15 (2013) 8613–8622, https://doi.org/10.1039/C3CE41178H.
[60] T. Miura, K. Sato, H. Nakamura, The role of microcracking on the compressive strength and stiffness of cracked concrete with different crack widths and angles evaluated by DIC, Cem. Concr. Compos. 114 (2020) 103768, https://doi.org/10.1016/j.cemconcomp.2020.103768.
[61] Z. Aly, E.R. Vance, D.S. Perera, J.V. Hanna, C.S. Griffith, J. Davis, D. Durce, Aqueous leachability of metakaolin-based geopolymers with molar ratios of Si/Al = 1.5–4, J. Nucl. Mater. 378 (2008) 172–179, https://doi.org/10.1016/j.jnucmat.2008.06.015.
[62] J. Liu, J.-H. Doh, D.E.L. Ong, S. Wang, Y. Yang, H.L. Dinh, G. Zi, Correlation between dissolubilities of Si, Al, and Fe from aluminosilicate precursor and strength of fly ash-based geopolymer, Construct. Build Mater. 393 (2023) 132107, https://doi.org/10.1016/j.conbuildmat.2023.132107.
[63] Z. Sun, A. Vollpracht, Leaching of monolithic geopolymer mortars, Cem. Concr. Res. 136 (2020) 106161, https://doi.org/10.1016/j.cemconres.2020.106161.
[64] T.M. Holden, Neutron diffraction, Pract. Residual Stress Meas. Methods (2013) 195–223, https://doi.org/10.1002/9781118402832.ch8.